Title: Unraveling the immunological roles of murine serum amyloid A3 in aortic immune cell subsets during atherosclerosis progression

Authors: Tzu-Yin Chou[1,2], Yu-Zhen Ye[1,2], Chia-Jung Lien[1], Jui-Chun Wang[1], Chen-Hsuan Yang[1], Yen-Ting Chen[1], I-Jung Lin[1], Pei-An Chao[1], Jian-Da Lin[1]*

Affiliations:

[1]Department of Biochemical Science and Technology, National Taiwan University, Taipei 10617, Taiwan

[2]These authors contributed equally.

* Correspondence to:

jdlin@ntu.edu.tw

Abstract

Atherosclerosis is a growing concern in developed nations, necessitating the identification of therapeutic targets for advancing personalized medicine. Serum amyloid A3 (*Saa3*) has been linked to accelerated plaque progression by affecting cholesterol metabolism and modulation of inflammation. We hypothesize that knocking out *Saa3* (*Saa3*$^{-/-}$) could mitigate plaque development by regulating aortic immune cell compositions during atherosclerosis progression. Using a murine model, we induced atherosclerosis via a gain-of-function mutant PCSK9-encoding adeno-associated viral vector (AAVmPCSK9) in wild-type (WT) and *Saa3*$^{-/-}$ mice. *Saa3*$^{-/-}$ mice developed smaller plaques than WT mice, and single-cell RNA sequencing revealed significant differences in aortic immune cell populations, particularly among aortic macrophages. Aortic macrophages in atherosclerotic *Saa3*$^{-/-}$ mice represent an anti-inflammatory and tissue-repairing phenotype and the Trem2^{hi} macrophages, characterized by high *Gpnmb*, *Lpl*, and *Spp1* expressions, predominated over the typical resident foamy macrophages in *Saa3*$^{-/-}$ compared to WT mice. Notably, SAA3 regulates cholesterol metabolism and inflammatory responses in foamy macrophages. Our study highlights *Saa3* as a key modulator of aortic immune cells that impact atherosclerosis progression.

35 ## Introduction

36 Atherosclerosis, a major cardiovascular concern in developed countries [1], is a chronic
37 arterial disease characterized by plaque formation within arterial walls. This process
38 involves complex interplays among various cellular components and inflammatory
39 mediators that drive inflammation and lipid accumulation. Atherosclerosis initiation
40 involves low-density lipoprotein (LDL) accumulation in the coronary artery intima,
41 which upon oxidation to ox-LDL by risk factors, activates nuclear factor kappa B (NF-
42 κB) [2,3]. This leads to the expression of adhesion molecules like vascular cell adhesion
43 molecule-1 (VCAM-1) and intercellular adhesion molecule-1 (ICAM-1) on the
44 endothelium, aiding monocyte recruitment into the vascular wall [4]. These recruited
45 monocytes then convert into macrophages under the influence of macrophage colony-
46 stimulating factor (M-CSF), and release inflammatory cytokines such as interleukin
47 (IL)-1β, IL-12, and tumor necrosis factor (TNF)-α, escalating the inflammatory
48 response[5]. As the disease progresses, these macrophages become foam cells by
49 uptaking ox-LDL, which is crucial for plaque formation and intimal thickening.

50 Macrophages are the predominant type of immune cell found in aortic plaques but
51 display a wide range of phenotypes and functions. At the onset of atherosclerosis,
52 macrophages ingest ox-LDL via receptors like CD36 and SR-A, forming cholesterol-

53 rich foam cells. Continued lipid intake without effective cholesterol removal leads to
54 foam cell death, creating a necrotic core in advanced plaques [6,7]. Single-cell RNA
55 sequencing (scRNA-seq) of monocyte-derived macrophages has revealed that
56 macrophage heterogeneity is beyond M1/M2 definitions and associated with different
57 states of atherosclerosis, where progression is linked to more complex states than
58 regression [8]. This technique has revealed various macrophage subsets within
59 atherosclerotic plaques, each characterized by unique markers and roles contributing
60 to aortic plaque progression or regression. Notably, three main groups are identified:
61 tissue-resident-like macrophages, marked by *Folr2* and *Lyve1*, which promote tissue
62 stability; inflammatory macrophages, with markers such as *Tnf* and *Il1b*, which
63 activate immune responses; and anti-inflammatory TREM2^{hi} macrophages, associated
64 with cholesterol metabolism and identified by markers such as *Trem2* [9,10]. This
65 diversity in macrophage functions underscores the complexity of atherosclerosis and
66 offers multiple targets for therapy.
67 The Serum Amyloid A (SAA) protein family, encompassing SAA3 as one of its
68 members, represents a class of acute phase proteins pivotal in immune responses.
69 Previous studies suggest that *Saa3* has a modulatory role in local injury and
70 inflammatory responses, as the expression of *Saa3* at the mRNA or protein level in
71 mouse macrophages increases with the administered dosage of lipopolysaccharide

72 (LPS) [11]. It also indicates that increased SAA expression correlates with the aortic

73 plaque progression in *ApoE*$^{-/-}$ mice, accompanied by elevated levels of IL-6 and

74 TNF-α. This upregulation potentially facilitates the infiltration of M1 macrophages

75 into atherosclerotic regions, thereby promoting atherosclerosis progression [12]. *Saa3* is

76 actively expressed, predominantly in macrophages and adipose tissues [13], and the

77 activation of the *Saa3* promoter is regulated through C/EBPβ signaling, which in turn

78 activates macrophages, underscoring the complex interaction within adipose tissue [14].

79 Pulmonary exposure to nanoparticles induces pronounced acute phase responses, with

80 *Saa3* identified as the most differentially regulated gene, demonstrating prolonged

81 upregulation in lung tissue and correlating with neutrophil infiltration and systemic

82 SAA3 protein levels[15]. Notably, SAA3 has been reported to promote atherosclerosis,

83 and overexpressed SAA3 increases atherosclerotic plaque size [16]. Overall, these

84 studies support the role of SAA3 in regulating macrophage function during

85 atherosclerosis, though the specific type of aortic macrophages that regulate aortic

86 plaque progression and the underlying mechanisms remain elusive.

87 To assess how *Saa3* deficiency impacts aortic immune cell composition and

88 functionalities in contributing to atherosclerosis progression, we applied scRNA-seq

89 using the BD Rhapsody platform on immune cells from aortic arches of *Saa3*

90 knockout (*Saa3*$^{-/-}$) mice and littermate wild-type (WT) control mice during

91 atherosclerosis. Our investigation seeks to delineate the impact of *Saa3* deficiency on
92 the phenotypic and functional landscape of aortic macrophages and other immune cell
93 populations. By comparing the immune cell profiles between *Saa3*$^{-/-}$ and WT mice,
94 we aim to uncover the molecular mechanisms by which SAA3 influences macrophage
95 or other immune cell types-mediated aortic plaque progression.
96

97 ## Results

98 ### *Saa3* deletion reduced aortic plaque progression but increased peripheral lipid
99 levels

100 To determine the phenotype of atherogenesis after *Saa3* deficiency, we utilized a
101 C57BL/6 wild-type (WT) mouse-based atherosclerosis model independent of *Ldlr*$^{-/-}$
102 mice breeding [8,17,18]. Plaque progression was initiated by injecting the mice with an
103 adeno-associated viral vector expressing a gain-of-function mutant of protein
104 convertase subtilisin/kexin type 9 (AAVmPCSK9), resulting in LDL receptor
105 deficiency and hypercholesterolemia. Both C57BL/6 WT and C57BL/6 *Saa3*$^{-/-}$ mice
106 were treated with AAVmPCSK9 and fed the Western diet (WD) for 18 weeks to
107 induce hypercholesterolemia and aortic plaque formation. We longitudinally collected
108 plasma from mice at 0, 2, 4, 8, 12, and 16 weeks on WD, and the immune profiling
109 was performed on sorted CD45+ cells from aortic arches by single-cell RNA-seq at
110 18 weeks on WD (Fig. 1a). We first determined total cholesterol levels in the plasma
111 of WT and *Saa3*$^{-/-}$ mice and a baseline comparison at weeks 0 revealed no significant

112 differences, with levels below 100 mg/dL (Fig. 1b). Over time, *Saa3*$^{-/-}$ mice
113 developed higher cholesterol levels than WT, with a slight increase at weeks 2
114 through 12, and a significant rise by weeks 16 (Fig. 1b).
115 Research demonstrates that serum amyloid A (SAA) attenuates the anti-
116 inflammatory and antioxidative functions of high-density lipoprotein (HDL) by
117 facilitating its binding to adipocyte and macrophage-derived glycoproteins[19]. We
118 conducted high-density lipoprotein (HDL)/ low-density lipoprotein LDL analyses that
119 revealed an increase in peripheral HDL levels during the initial phase of
120 atherosclerosis progression (Fig. 1c). Not only did HDL levels demonstrate a rising
121 trend with statistically significant increases in the *Saa3*$^{-/-}$ group compared to WT at
122 weeks 2 and 4, but the absence of *Saa3* also correlated with a potential increase in
123 LDL levels in the bloodstream (Fig. 1c).
124 Overexpression or suppression of SAA3 can increase or decrease aortic lesion area
125 in *ApoE*$^{-/-}$ mice[16]. We also determined aortic plaque sizes between WT and *Saa3*$^{-/-}$
126 mice by histologically evaluating aortic root sections stained with Oil Red O (Fig.
127 1d). It demonstrated a significant decrease in plaque area in *Saa3*$^{-/-}$ compared to WT
128 mice, with mean values of 31.50% and 45.48%, respectively (Fig. 1e). These
129 observations demonstrate that *Saa3* deficiency increases peripheral lipid levels but
130 attenuates aortic plaque formation, suggesting the complex roles of *Saa3* in
131 modulating lipid metabolism and atherogenesis.
132
133 ***Saa3* deficiency alters intercellular immune communications in aortic arches**

134 **during atherosclerosis progression**

135 All immune cells express CD45, a major transmembrane glycoprotein expressed on
136 all hematopoietic cells[20] and some cardiac fibroblasts[21]. To elucidate the
137 immunological impact of *Saa3* deficiency within the aortic arch and its putative role
138 in the pathogenesis of atherosclerosis, we performed a single-cell RNA sequencing on
139 FACS-purified CD45+ cells (Supplementary Fig. 1). After data processing, possible
140 contaminated cell removement, anchor-based dataset integration[22], and cell clusters
141 visualized by Uniform Manifold Approximation and Projection (UMAP), it revealed
142 the immune cell compositional variances in aortic arches between WT and *Saa3*$^{-/-}$
143 mice during atherosclerosis progression (Fig. 2). Utilizing the cell annotation tool by
144 *SingleR*[23], we classified the cell phenotypes, enabling initial taxonomical segregation
145 within the distinct clusters (Fig. 2a). Our analysis identified 9 cell subpopulations,
146 encompassing B cells, dendritic cells (DCs), innate lymphoid cells (ILCs),
147 macrophages, monocytes, neutrophils, natural killer T (NKT) cells, T cells, and γδ T
148 cells (Tgd) (Fig. 2a). Despite similar UMAP topologies between WT and *Saa3*$^{-/-}$
149 aortic cell populations (Fig. 2a), *Saa3*$^{-/-}$ mice showed increased T cells, B cells,
150 monocytes, γδ T cell, and neutrophils proportions but decreased macrophages, innate
151 lymphoid cells (ILC), and NKT cells compared to WT mice (Fig. 2b). Heatmaps of
152 differential gene expression profiles supported these *SingleR*-annotated cell type
153 differences, highlighting the top 5 marker genes per subset (Fig. 2c).

154 *Cellchat* has been used to infer, analyze, and visualize cell-cell communication
155 networks in scRNA-seq datasets[23]. To dissect the variances in signaling dynamics in
156 aortic cell types between WT and *Saa3*$^{-/-}$ mice, we employed *CellChat* to evaluate the
157 intercellular communication networks and assess the number and intensity of cellular
158 interactions within the respective cohorts (Figs. 2d-2e). The resultant metrics

159 demonstrated 1,822 and 1,787 interactions across all cell types in aortic arches
160 between WT and *Saa3*$^{-/-}$ mice, with interaction strength for *Saa3*$^{-/-}$ cell types
161 quantified at 83.957 compared to 64.762 for WT (Fig. 2d). To rigorously dissect the
162 discrete intercellular communication patterns responsible for the observed differential
163 signaling, we interrogate the heatmaps that delineate both the frequency and
164 magnitude of interaction strengths across aortic cell types (Fig. 2e). Increased
165 magnitude of intercellular interaction strengths was observed in the aortic arches of
166 *Saa3*$^{-/-}$ mice compared to their WT mice (Fig. 2d). The increased interaction
167 magnitudes were primarily directed from most immune cells toward γδ T cells (Tgd),
168 while reduced interactions were directed from macrophages toward other immune
169 cells in *Saa3*$^{-/-}$ mice compared to WT mice (Fig. 2e). These patterns suggest that the
170 absence of the *Saa3* gene exerts a profound regulatory influence on the intercellular
171 communication network among immune cells, potentially revealing critical insights
172 into the regulatory mechanisms of immune function within the aortic niche.
173

174 ***Saa3* depletion increases biological processes in aortic macrophages that are**
175 **highly associated with lipid metabolism and inflammatory recruitment during**
176 **atherosclerosis**

177 *CellChat* analysis revealed significant differences in cell-cell interaction signals
178 between aortic macrophages and other aortic immune cell populations within the
179 *Saa3*$^{-/-}$ and WT group (Figs. 2e-2f). To delve deeper, we assessed the transcriptomic
180 variances in macrophages from *Saa3*$^{-/-}$ versus WT mice. Our volcano plot delineated
181 distinct gene expression profiles, with genes such as *Fabp5* and *Gpnmb* are
182 upregulated in *Saa3*$^{-/-}$ mice, exceeding the established $\log_2$ fold change threshold of

183 >1 and p-values < 0.01 (Fig. 2f). *Fabp5*, which plays a central role in the intracellular
184 transport of lipids, is integral to the uptake, transport, and metabolism of fatty acids.[24]
185 *Gpnmb* has been shown to protect against obesity-related metabolic disorders by
186 mitigating macrophage inflammatory capacity[25]. Conversely, genes such as *Cxcl13*,
187 *Lyz1*, *Tmem176a*, *Clec4a1*, *C3*, and *Cfp* are downregulated in *Saa3*$^{-/-}$ macrophages
188 (Fig. 2f). Studies have demonstrated that a lack of *Cxcl13* correlates with a
189 diminished presence of atherosclerotic conditions, likely due to lower recruiting
190 inflammatory granulocytes within the lesions [26 27]. *C3* expression in macrophages has
191 been linked to exacerbating atherosclerosis by limiting macrophage efferocytosis,
192 contributing to plaque development and inflammation.[28] *Cfp* has been linked to
193 regulating complement activation and orchestrating iron homeostasis[29]. Gene set
194 enrichment analysis, conducted using the *ClusterProfiler* package[30], revealed distinct
195 gene ontology (GO) pathways in aortic macrophages (Fig. 2g). WT aortic
196 macrophages were enriched for pathways associated with enhanced immune cell
197 recruitment and chemotaxis, whereas *Saa3*$^{-/-}$ aortic macrophages exhibited enrichment
198 for pathways related to lipid localization and transport (Fig. 2g, Supplementary Table
199 1). Overall, these data suggest the phenotypes of aortic macrophages were impacted
200 by reduced recruitment of inflammatory macrophages, which helped mitigate
201 inflammation potentially influencing lesion formation and stability.
202

203 **Altered macrophage compositions and enhanced Trem2^{hi} macrophage presence**
204 **linked to diminished aortic plaque progression in *Saa3*$^{-/-}$ mice**

205 Macrophage (Mφ) polarization, along with several distinct clusters, has been
206 identified as increasingly prevalent during the atherosclerosis progression than

207 regression[8,31]. To dissect the functional heterogeneity of aortic macrophage
208 populations in WT and *Saa3*$^{-/-}$ mice during atherosclerosis, we classified macrophages
209 into subpopulations and compared the top differentially expressed genes from each
210 cluster against our previously published dataset, where we profiled single-cell sorted
211 *Cx3cr1*-derived aortic macrophages from lineage-tracing mice during atherosclerosis
212 progression and regression (hereinafter referred to as "*Lin regression study*")[8]. There
213 are five distinct macrophage clusters in the aortic arches of WT and *Saa3*$^{-/-}$ mice
214 during atherosclerosis (Fig. 3a). CD74^{hi}MHCII^{hi} Mφ is the most abundant
215 macrophage subset in both genotypes, with CD74^{hi}MHCII^{hi}, Folr2^{hi}, and
216 Retnla^{hi}Ear2^{hi} Mφ being more prevalent in WT mice compared to *Saa3*$^{-/-}$ mice (Fig.
217 3b). Conversely, Trem2^{hi} and Apbb2^{hi} Mφ are found in higher percentages within the
218 aortic arches of *Saa3*$^{-/-}$ mice than WT mice (Fig. 3b).
219 The Cd74^{hi}MHCII^{hi} Mφ, a subset identified through the *Lin regression study*[8], is
220 characterized by high expression of genes such as *Tmem176b*, *Lilra5*, *H2-Eb1*, and
221 *H2-Aa* (Supplementary Fig. 2a and Table 2). Folr2^{hi} Mφ exhibit unique transcriptional
222 profiles with *F13a1, Pf4, Folr2*, and *Lyve1* (Supplementary Fig. 2a and Table 2).
223 These markers are indicative of a tissue-resident-like macrophage phenotype[32-35] and
224 align with the molecular signature of the Folr2^{hi} macrophage cluster previously
225 delineated in the *Lin regression study* [8]. Retnla^{hi}Ear2^{hi} Mφ is distinguished by their
226 elevated expression of genes such as *Retnla* and *Ear2*, which suggest an early-stage
227 transition of monocytes to macrophages within tissues[36,37]. Additionally, these
228 macrophages show enrichment in genes like *Gm2a* and *Fn1*, confirming their
229 specialized state as identified in the *Lin regression study*[8]. Trem2^{hi} Mφ is defined by a
230 gene expression signature that mirrors the population described by *Cochain et al.*[38]
231 and *Lin regression*[8] studies and is exemplified by heightened expression of *Ctsd,*

232 *Lgals3, Spp1*, and *Lpl* (Supplementary Fig. 2a and Table 2). Apbb2^{hi} Mφ is
233 characterized by the predominant expression of *Cd9, Cd72*, and *Hexb* genes. While
234 sharing traits with the "Trem2^{hi} Mφ," they are uniquely distinguished by their
235 expression of *Apbb2* (Supplementary Fig. 2a and Table 2).
236 On the other hand, we identified differentially expressed genes (DEGs) across five
237 macrophage populations and conducted gene ontology (GO) enrichment analysis on
238 biological pathways to explore potential functions (Supplementary Fig. 2b and Table
239 3). Compared to other macrophage clusters, Cd74^{hi}MHCII^{hi} Mφ in the aortic arches
240 showed significant enrichment in pathways related to leukocyte-mediated immunity,
241 positive regulation of cell activation, activation of the immune response, and
242 immunoglobulin-mediated immune responses (Supplementary Fig. 2b and Table 3).
243 Folr2^{hi} Mφ is distinguished by activation of immune response, ameboidal-type cell
244 migration, cell chemotaxis, regulation of angiogenesis, and regulation of viral
245 processes (Supplementary Fig. 2b and Table 3). Retnla^{hi}Ear2^{hi} Mφ were noted for
246 their leukocyte proliferation, mononuclear cell proliferation, positive regulation of
247 leukocyte cell-cell adhesion, positive regulation of T cell activation, and response to
248 type II interferon (Supplementary Fig. 2b and Table 3). Trem2^{hi} Mφ is characterized
249 by the generation of precursor metabolites and energy, aerobic respiration, oxidative
250 phosphorylation, purine ribonucleoside triphosphate biosynthetic process, and ATP
251 biosynthetic process (Supplementary Fig. 2b and Table 3). These functions highlight
252 the metabolic specialization of Trem2^{hi} Mφ in energy production and biosynthesis.
253 Apbb2^{hi} Mφ demonstrated upregulation in myeloid cell differentiation, leukocyte
254 migration, actin filament organization, regulation of protein-containing complex
255 assembly, and mononuclear cell migration (Supplementary Fig. 2b and Table 3).

256 In *Lin regression study*[8], Cd74^{hi}MHCII^{hi} Mφ and Retnla^{hi}Ear2^{hi} Mφ are abundant in
257 aortic arches of progression group and we also observed these two subsets are higher
258 in aortic arches of WT mice compared to *Saa3*$^{-/-}$ mice (Fig. 3b). *Folr2* expression is
259 increased in human atherosclerotic plaques compared to normal arterial tissue[39] and
260 we also observed aortic Folr2^{hi} Mφ are higher in WT mice than *Saa3*$^{-/-}$ mice (Fig. 3b).
261 Trem2^{hi} Mφ exhibits comparable prevalence between the progression and regression
262 cohorts in the *Lin regression study*[8], whereas both Trem2^{hi} and Apbb2^{hi} Mφ are more
263 abundant in the aortic arches of *Saa3*$^{-/-}$ mice compared to WT mice (Fig. 3b). Trem2^{hi}
264 Mφ is previously identified as lipid-laden foam cells within atherosclerotic lesions,
265 underscoring their capacity for lipid processing and phagocytosis[9,10,31]. They are
266 associated with anti-inflammatory responses, which may help prevent the
267 establishment of a proinflammatory environment within the plaque[9,31,40]. Similar to
268 previous findings, Trem2^{hi} Mφ expresses high *Spp1,* a gene associated with fibrotic
269 responses indicative of tissue repair mechanisms[41,42] (Fig. 3c, Supplementary Fig. 2a).
270 Additionally, this subset expresses *Gpnmb*, a gene implicated in anti-inflammatory
271 processes[25,43], along with *Fabp5*, which is involved in the uptake and transport of
272 fatty acids[24] (Fig. 3c). Notably, enzymes such as *Lpl*, central to lipid metabolism[44] ,
273 and *Mmp12*, a contributor to extracellular matrix remodeling[45], further characterize
274 this population (Fig. 3c). Hence, these data indicate that *Saa3*$^{-/-}$ mice exhibit higher
275 compositions of aortic macrophages with tissue-repairing and anti-inflammatory
276 properties, leading to reduced aortic plaque progression.
277

278 ***Saa3* modulates aortic macrophage functionalities during atherosclerosis**

279 Investigating the transition of macrophage phenotypes from M1-like to M2-like as a
280 therapeutic strategy recognizes the complexity of aortic macrophage phenotypes in
281 atherosclerosis, which extend beyond conventional M1 and M2 polarization states[8,31].
282 We use typical markers for Chemokine, Interferon (IFN), Inflammatory, and Type II
283 responses to visualize the aortic macrophage subsets from WT and *Saa3*$^{-/-}$ mice (Fig.
284 3d). Among the comparisons between WT and *Saa3*$^{-/-}$ aortic Mφ, pronounced
285 differences were noted in the increased expression levels of chemokines including
286 *Cxcl1*, *Ccl2*, *Ccl3*, and *Ccl4* in *Saa3*$^{-/-}$ than WT Folr2^{hi} Mφ (Fig. 3d). Chemokines are
287 signaling molecules that attract various types of immune cells to sites of infection or
288 injury. Increased expression of chemokines by tissue-resident macrophages enhances
289 the recruitment of neutrophils and lymphocytes, which is crucial for initiating and
290 sustaining an effective immune response[46]. Additionally, there was a higher
291 expression of type II response markers including *Cd163, Mrc1*, and *Msr1*[47-50] in *Saa3*$^{-}$
292 $^{/-}$ than WT Folr2^{hi} Mφ (Fig. 3d). Moreover, Il10ra showed higher expression in *Saa3*$^{-/-}$
293 than WT Cd74^{hi}MHCII^{hi} Mφ, and Il10ra is required for protection against
294 atherosclerosis in low-density lipoprotein receptor knockout mice[51]. Furthermore, we
295 observed higher expression levels of interferon regulatory and downstream markers
296 such as *Irf5*, *Irf7*, *Isg15*, and *Stat1* in WT than *Saa3*$^{-/-}$ Retnla^{hi}Ear2^{hi} Mφ (Figure 3d),
297 which may indicate an enhanced interferon response in these cells [52,53]. These
298 expression patterns indicate a significant alteration in gene expression profiles and
299 macrophage composition between the two genotypes, suggesting that deletion of the
300 *Saa3* may modulate macrophage recruitment, type 2 immune responses, and
301 inflammatory/anti-inflammatory phenotypes.
302

303 ***Saa3* modulates aortic macrophage communications that impact inflammatory**
304 **processes**

305 To determine the role of *Saa3* in aortic macrophage communication during
306 atherosclerosis, we also performed a comparative analysis of cell interactions using
307 *CellChat*[23] in both WT and *Saa3*$^{-/-}$ macrophages. Our findings indicate a substantial
308 decline in intercellular communication in *Saa3*$^{-/-}$ macrophages, with interaction events
309 decreasing from 482 in WT to 290 in *Saa3*$^{-/-}$ cells (Fig. 3e). Correspondingly, we
310 observed a significant drop in the strength of these interactions, with the average
311 interaction strength in WT macrophages being 17.997 compared to a lower average of
312 14.348 in *Saa3*$^{-/-}$ macrophages, mirroring the decrease in the number of interaction
313 events (Fig. 3e).

314 The heatmap depicts the overall signaling patterns observed in various macrophage
315 subpopulations from WT and *Saa3*$^{-/-}$ mice (Fig. 3f), and the bar graph shows the
316 relative information flow of these signaling pathways between WT and *Saa3*$^{-/-}$
317 macrophages (Fig. 3g). In the context of inflammatory-mediated atherosclerosis
318 progression, WT macrophages present higher signaling activity in THBS, ANGPTL,
319 LAMININ, PVR, CD226, OSM, NOTCH, CADAM, and JAM pathways compared to
320 *Saa3*$^{-/-}$ macrophages (Figs. 3f-3g). In THBS signaling, *Thbs1* is a critical regulator of
321 macrophage interleukin-1β (IL-1β) production and activation via CD47, highlighting
322 the complex interplay between thrombospondins and immune modulation[54]. In
323 ANGPTL signaling, ANGPTL2 promotes vascular inflammation and accelerates
324 atherosclerosis progression, with increased cardiac ANGPTL2 production linked to
325 heart failure and pathological cardiac remodeling by influencing inflammatory
326 responses and affecting both cardiomyocytes and macrophages[55,56]. In LAMININ and
327 JAM signaling, LAMININ and junctional adhesion molecules (JAM) are involved in

328 monocyte-to-macrophage differentiation and macrophage migration, playing roles in
329 immune cell dynamics and atherosclerotic disease modulation[57,58]. PVR significantly
330 contributes to atherosclerosis by facilitating leukocyte migration across the
331 endothelium, thereby promoting inflammation [59]. When loss of CD226, a
332 costimulatory molecule, has been observed to protect against atherosclerosis by
333 preventing foam cell formation and reducing plaque buildup[60]. Oncostatin M (OSM)
334 signaling promotes atherogenesis and plaque vulnerability by promoting the
335 differentiation of vascular smooth muscle cells into osteoblastic phenotypes via M1
336 macrophages, potentially leading to plaque instability [31]. NOTCH signaling plays a
337 significant role in atherosclerosis development, with *Notch-1* deletion inducing anti-
338 inflammatory M2 effects through the PI3K-Akt pathway, contrasting with its
339 increased presence in vulnerable human plaques [61].
340 In contrast to their WT counterparts, *Saa3*$^{-/-}$ macrophages exhibit elevated
341 expression of signaling molecules such as COLLAGEN, GRN, SN, TGFb, and
342 CLEC. Collagen plays a crucial role in modulating macrophage functions and
343 improving plaque stability, with an increased presence in M2-polarizing macrophages
344 within the plaque [62,63]. GRN exerts anti-atherogenic effects by enhancing nitric oxide
345 production in endothelial cells through the Akt/eNOS signaling pathway, forming a
346 complex with apolipoprotein A-I to stabilize atherosclerotic plaques. In addition, in
347 atherosclerotic mice, its deficiency leads to increased expression of adhesion
348 molecules and inflammatory cytokines [64-66]. TGF-β signaling contributes to the
349 reduction and stabilization of atherosclerotic plaques by altering macrophage
350 functions, and its overexpression is linked to smaller lesions, increased collagen
351 deposition, smooth muscle cell infiltration, and reduced macrophage presence,
352 ultimately fostering a more stable lesion phenotype[67]. CLEC signaling, specifically

353 through Clec4a2, a C-type lectin receptor, protects against atherosclerosis by
354 promoting homeostatic functions within the vessel wall, enhancing cholesterol
355 metabolism, and limiting immune responses to toll-like receptors [68]. In summary, this
356 analysis confirms that aortic macrophages in WT mice are more associated with
357 inflammatory and migration processes, whereas aortic macrophages in *Saa3*$^{-/-}$ mice
358 are more related to vascular protection and aortic plaque stabilization.
359

360 **Differential effects of *Saa3* deficiency on macrophage subpopulations and ligand-**
361 **receptor interactions**

362 We further investigated the differential effects of *Saa3* deficiency on five
363 macrophage subpopulations. Our observations revealed that, aside from Trem2^{hi} Mφ,
364 the gene expression profiles of CD74^{hi}MHCII^{hi} Mφ, Folr2^{hi} Mφ, Retnla^{hi}Ear2^{hi} Mφ,
365 and Apbb2^{hi} Mφ in *Saa3*$^{-/-}$ mice exhibited substantial downregulation of numerous
366 genes when compared to their WT counterparts (Figs. 4a-4d). We also performed GO
367 term enrichment pathway analysis on the downregulated DEGs in these four *Saa3*$^{-/-}$
368 macrophage subpopulations compared to WT (Figs. 4e-4h). The analysis revealed
369 common downregulated genes in *Saa3*$^{-/-}$ mice, including *Lyz1*, *Lyz2*, other lysozyme-
370 related genes, *Cxcl13*, and *Ccl8*, which are associated with pathways involved in cell
371 killing and the destruction of other organisms, suggesting that the absence of *Saa3*
372 impairs macrophage functions in combating pathogens as previous studies[69,70] (Figs.
373 4e-4h). Specifically, Folr2^{hi} Mφ in *Saa3*$^{-/-}$ mice showed significant downregulation of
374 *Cxcl13* (Fig. 4b). Previous study indicates patients with carotid atherosclerosis exhibit
375 elevated plasma levels of CXCL13, especially in symptomatic cases, and higher
376 CXCL13 expression within atherosclerotic carotid plaques compared to non-
377 atherosclerotic vessels[71]. CCL8 is a potent chemoattractant for monocytes and

378 macrophages, directing them to areas of inflammation and infection[72,73].
379 Retnla^{hi}Ear2^{hi} Mφ in WT mice show higher enrichment in ERK1 and ERK2 cascade,
380 positive regulation of angiogenesis, and lipid storage (Figs. 4c, 4g). ERK1 and ERK2
381 signaling pathways regulate macrophage function in atherosclerosis. Deletion of *Erk1*
382 reduces macrophage migration and plaque lipid content in LDL receptor-deficient
383 mice on a high-fat diet[74,75]. Apbb2^{hi} Mφ in WT mice enrich in defense response to
384 virus and interferon (Figs. 4d, 4h). This may indicate that Apbb2^{hi} Mφ in WT mice
385 has more inflammatory response features than in *Saa3*$^{-/-}$ mice, contributing to chronic
386 inflammation, plaque instability, and progression [76]. To elucidate the specific ligand-
387 receptor interactions contributing to the observed differences in pathway patterns
388 between *Saa3*$^{-/-}$ and WT groups, we conducted a comparative analysis of ligand-
389 receptor signaling within five subpopulations of macrophages (Supplementary Figs
390 3a-3e). The analysis encompassed an assessment of the differential expression of
391 ligands and receptors and the computation of interaction probabilities, thereby
392 enabling the dissection of signaling discrepancies between the two genotypic
393 conditions. Since aortic Trem2^{hi} Mφs are more abundant in *Saa3*$^{-/-}$ mice, we focus on
394 ligand-receptor interactions within Trem2^{hi} Mφ under both WT and *Saa3*$^{-/-}$ conditions
395 (Supplementary Fig. 3d). Prominently, pairs such as Spp1-Cd44 and Spp1-integrins
396 (Itgav+Itgb1, Itga5+Itgb1, Itga4+Itgb1), exhibit a heightened probability of
397 interaction in the signal transduction pathways of Trem2^{hi} Mφ within the *Saa3*$^{-/-}$ mice
398 (Supplementary Fig. 3d). Spp1 is established to bind integrins Itgav, Itgb1, Itgb5, and
399 Itga4 (Col4a2-Sdc44, Col4a2-Cd44, Col4a2-(Itga9+Itgb1), Col4a1-Sdc44, Col4a1-
400 Cd44, Col4a1-(Itga9+Itgb1)), influencing cellular adhesion and migration
401 crucially[77,78] (Supplementary Fig. 3d). Furthermore, interactions involving Col4a2
402 and Col4a1 with their partners are exclusively observed in the *Saa3*$^{-/-}$ condition

403 (Supplementary Fig. 3d). As major constituents of the basement membrane, type IV
404 collagen may have implications for the stability of atherosclerotic plaques.[79] In
405 contrast, the CCL-CCR signaling axis, encompassing Ccl9-Ccr1, Ccl8-Ccr1, Ccl7-
406 Ccr1, Ccl6-Ccr2, Ccl6-Ccr1, Ccl3-Ccr5, and Ccl3-Ccr1, is exclusively active in the
407 WT condition within Trem2^{hi} Mφ transitioning to Retnla^{hi}Ear2^{hi} Mφ (Supplementary
408 Fig. 3d). These chemokine-mediated communications facilitate the recruitment of
409 macrophages or monocytes to sites of inflammation, contributing to the formation and
410 progression of atherosclerotic lesions and plaque vulnerability[80,81]. Parallel
411 observations were noted for the ligand-receptor pairs Cd74^{hi}MHCII^{hi} Mφ, Folr2^{hi} Mφ,
412 Retnla^{hi}Ear2^{hi} Mφ, and Apbb2^{hi} Mφ to Retnla^{hi}Ear2^{hi} Mφ (Supplementary Figs. 3a-
413 3e). It is posited that these altered signaling patterns may underlie the observed
414 reductions in plaque burden and macrophage recruitments in *Saa3*$^{-/-}$ mice.
415
416 **Trem2^{hi} Mφ potentially mitigates aortic plaque development by enhancing lipid**
417 **absorption, promoting an anti-inflammatory environment, and increasing**
418 **extracellular matrix and fibrosis.**
419 In atherosclerosis, *Saa3* deletion precipitates substantial changes in macrophage gene
420 expression profiles, within the Trem2^{hi} Mφ, as evidenced by differential expression
421 between WT and *Saa3*$^{-/-}$ groups (Fig. 5a). The upregulation of genes in *Saa3*$^{-/-}$ than
422 WT Trem2^{hi} Mφ such as *Fabp4, Fabp5,* and *Lpl*, which are central to lipid
423 metabolism[82,83], as well as *Ctsk*, has been implicated in promoting disturbed flow-
424 induced endothelial inflammation.[84] Other genes including *Gpnmb, Atp6v0d2, Mrc1,*
425 *Mmp12*, and *Spp1* also exhibit altered expression (Fig. 5a). Studies suggest that
426 *Gpnmb* may be anti-inflammatory by promoting inflammation resolution, as it can
427 attenuate pro-inflammatory responses and promote M2 polarization in

428 macrophages[43,85,86]. The suppression of *Gpnmb* has been associated with enhanced
429 atherosclerotic plaque formation, whereas its overexpression correlates with
430 decreased plaque development[87]. Augmented *Atp6v0d2* expression activates
431 autophagy as a compensatory response to hemodynamic pressure, which indicates its
432 role in maintaining plaque stability and potentially curtailing the progression of
433 atherosclerosis[88,89]. *Mrc1* appears to modulate macrophage polarization toward an
434 anti-inflammatory phenotype[90], while *Mmp12* plays a pivotal role in attenuating
435 inflammation and fostering resolution via targeted proteolysis of chemokines[91,92].
436 Spp1+ foamy macrophages have been linked to signaling pathways that might abate
437 plaque progression and stabilize susceptible lesions[93]. These genes correspond to GO
438 enrichment pathways such as lipid localization, fatty acid transport, and the positive
439 regulation of macrophage-derived foam cell differentiation (Fig. 5b). These results
440 suggest that *Saa3*$^{-/-}$ Trem2^{hi} Mφ may possess enhanced lipid uptake and metabolism
441 capabilities, which could contribute to the significant reduction in plaque size.
442 Additionally, genes like *Ctsk*, *Gpnmb*, *Igf1*, and *Spp1* are associated with tissue
443 remodeling pathways, indicating a potential shift of *Saa3*$^{-/-}$ Trem2^{hi} Mφ towards an
444 anti-inflammatory phenotype (Fig. 5b). Differential gene expression analysis utilizing
445 violin plots demonstrated that genes associated with tissue repair and lipid
446 metabolism—specifically *Gpnmb*, *Fabp5*, *Lpl, Lgals3*, *Cd36*, *Spp1*, and *Pparg*—are
447 more prominently expressed in *Saa3*$^{-/-}$ Trem2^{hi} Mφ compared to their WT
448 counterparts (Fig. 5c). CD36 is a scavenger receptor widely expressed on the surface
449 of various cell types, including macrophages. CD36 binds to oxLDL particles,
450 facilitating their uptake into the macrophage, particularly in the context of
451 atherosclerosis and inflammation[94]. Concomitantly, there is a downregulation of
452 genes in *Saa3*$^{-/-}$ than WT Trem2^{hi} Mφ such as *Thbs1, Kdm7a, Vegfa, Slc7a11, Fn1*,

453 and *Chil3*. These genes correspond to GO enrichment pathways such as positive
454 regulation of chemotaxis, positive regulation of vasculature development, and
455 angiogenesis (Fig. 5b). Angiogenesis is associated with inflammatory cells and can
456 contribute to plaque instability[95,96]. This complex gene expression network
457 underscores the multifaceted influence of *Saa3* in atherosclerosis and pinpoints
458 interconnected genes geared toward modulating macrophage function to combat
459 disease progression.

460 Analysis of aortic Trem2^{hi} macrophages from WT and *Saa3*$^{-/-}$ mice also revealed a
461 consistent expression pattern for a cohort of genes associated with lipid metabolism
462 and cholesterol processing (Figs 5b-5c). The violin plots compare the expression
463 levels of genes central to cholesterol efflux pathways, including *Abca1, Abcg1,*
464 *Nr1h2, Scarb, Nr1h3*, and *Apoe* (Fig. 5c, Supplementary Fig. 4). There were no
465 statistically significant differences observed between the two genotypes for most
466 genes (Fig. 5c).

467 Analysis through *CellChat* has additionally revealed alterations in the growth
468 differentiation factor (GDF) signaling pathway in all subsets of the aortic
469 macrophages (Figs. 5d-5e). In the *Saa3*$^{-/-}$ Trem2^{hi} macrophage phenotype, there is a
470 notable shift towards the sender role in the GDF signaling network (Fig. 5d). In
471 contrast, Folr2^{hi} macrophages predominantly assume the signaling initiative in the
472 WT condition (Figs. 5d-5e). This shift in signaling behavior suggests that the absence
473 of *Saa3* leads to a reprogramming of the Trem2^{hi} macrophage population, endowing
474 them with a more prominent role in initiating signaling within the GDF pathway.
475 GDF-15 has been reported to reduce cardiac damage and rupture after myocardial
476 infarction by mitigating inflammation and apoptosis via the PI3K/Akt pathway. It also
477 protects against atherosclerosis by modulating apoptosis, inhibiting monocyte

478 recruitment and macrophage activation, and enhancing plaque stability[97-99]. Other
479 studies suggest GDF-15 may reduce macrophage accumulation in *Ldlr*$^{-/-}$ or *Apoe*$^{-/-}$
480 mice[100-102]. This shift in the gene expression landscape highlights the critical role of
481 *Saa3* in regulating macrophage function and may provide insight into the molecular
482 mechanisms underpinning the immune responses in aortic plaque progression.
483
484 **SAA3 modulates cholesterol efflux, synthesis, and inflammatory responses in**
485 **macrophages under steady-state condition or during foamy macrophage**
486 **differentiation**
487
488 SAA3 has been shown to exacerbate atherosclerosis in *ApoE*$^{-/-}$ mice, as evidenced by
489 increased lesion area upon overexpression and reduced disease severity with
490 suppression[16]. Another study also observed reduced aortic plaque lesions in
491 atherosclerotic *Saa3*$^{-/-}$*Ldlr*$^{-/-}$ mice and indicated that these effects are sex-dependent[103].
492 To validate our scRNA-seq observations on aortic macrophages and investigate the
493 role of *Saa3* in foamy macrophages, we performed qRT-PCR to assess the expression
494 of inflammatory genes (*Il1b* and *Tnf*), cholesterol efflux genes (*Abca1* and *Abcg1*),
495 and cholesterol synthesis genes (*Cyp51* and *Hmgcr*) in bone marrow-derived
496 macrophages (BMDMs) from WT and *Saa3*$^{-/-}$ mice (Fig. 6a). These BMDMs were
497 treated overnight with either media alone or 20 µg/ml soluble cholesterol to
498 differentiate cells into foamy macrophages (Fig. 6a). We also conducted scRNA-seq
499 analysis on WT BMDMs treated with SAA3 in either media alone or 20 µg/ml
500 soluble cholesterol (Fig. 6a). Overall, gender-specific effects were generally minimal
501 under these experimental conditions, while genes involved in cholesterol efflux and
502 synthesis were significantly lower in female WT foamy macrophages treated with

503 SAA3 compared to males (Figs. 6b-c). Consistent with the previous study[103], *Il1b*
504 expression was significantly upregulated in BMDMs from female *Saa3*$^{-/-}$ mice
505 compared to WT under media-alone conditions, with no such effect observed in male
506 mice, while *Tnf* expression remained unchanged between genotypes (Fig. 6b).
507 Following soluble cholesterol treatment, both WT and *Saa3*$^{-/-}$ BMDMs present
508 minimal differences, with upregulated expression of the cholesterol efflux gene
509 (*Abca1*) and downregulated expression of the cholesterol synthesis gene (*Cyp51*),
510 indicative of the foamy macrophage phenotype (Fig. 6c). SAA3 treatment
511 significantly reduced cholesterol efflux gene expression (*Abca1* and *Abcg1*) while
512 increasing cholesterol synthesis gene expression (*Hmgcr*) in WT BMDMs undergoing
513 foamy macrophage differentiation (Fig. 6c). We next performed scRNA-seq analysis
514 on SAA3-treated WT BMDMs to confirm that genes associated with tissue repair and
515 lipid metabolism (*Gpnmb*, *Lpl*, *Lgals3*, *Spp1*, *Cd36*, *Pparg*) were significantly
516 downregulated compared to untreated controls (Fig. 6d). This aligns with the *in vivo*
517 phenotypes, where Trem2^{hi} aortic macrophages from *Saa3*$^{-/-}$ mice exhibited
518 significantly higher expression of these genes compared to Trem2^{hi} macrophages
519 from WT mice (Figs. 5c, 6d). We further observed the genes associated with acute
520 inflammatory response, interferon responses, and cell chemotaxis are increased in
521 SAA3-treated WT BMDMs (Figs. 6e-6f). Notably, exogenous SAA3 significantly
522 increases *Il1b* expression in both foamy and non-foamy macrophages (Fig. 6b).
523 These data indicate that SAA3 modulates inflammatory and lipid metabolism
524 pathways in macrophages, particularly during foamy macrophage differentiation, by
525 reducing cholesterol efflux, increasing cholesterol synthesis, and enhancing
526 inflammatory and interferon responses, suggesting that SAA3 potentially exacerbates
527 atherosclerosis progression through these mechanisms.

528

529 **Discussion**

530 Humans do not express a functional SAA3 protein due to a premature stop codon in
531 the SAA3 gene, which results in a frameshift mutation and renders the human SAA3
532 gene a pseudogene[104]. Mouse SAA3 shares the highest amino acid homology (70%)
533 with human SAA1, and its tissue distribution and expression patterns, particularly in
534 adipose tissue, are more similar to human SAA1 than to mouse SAA1 or SAA2,
535 suggesting a functional similarity between mouse SAA3 and human SAA1[11].
536 Previous study indicates a significant upregulation of SAA3, but not SAA1 or SAA2,
537 in the adipose tissue of conventional mice compared to germ-free mice[105]. The
538 presence of intestinal microbiota significantly upregulated SAA3 expression in
539 adipose tissue and colonic tissue, with evidence indicating that its colonic regulation
540 is partially mediated through the Toll-like receptor (TLR)/MyD88/NF-κB signaling
541 axis[11]. Unlike SAA1 and SAA2, which are primarily expressed in the liver, intestine,
542 and kidneys, SAA3 is more broadly expressed across various mouse tissues[105]. In
543 humans, SAA1 is expressed in adipocytes, with its expression notably increased in
544 hypertrophic adipocytes of obese individuals[106]. These findings suggest that mouse
545 SAA3, which is upregulated in the adipose tissue of obese mice, may be functionally
546 analogous to human SAA1 and could represent a key link between low-grade
547 inflammation and obesity-related metabolic disorders. Additionally, the microbiota
548 likely plays a significant role in modulating the extent of these effects by
549 manipulating the SAA3 levels.

550 Gut microbiota plays a significant role in inducing and maintaining sex dimorphism,
551 particularly in relation to immune responses, metabolism, and hormone regulation. In
552 NOD mice, the sex difference in type 1 diabetes susceptibility disappears under germ-

553 free conditions, while gut microbiota transfer from males to females elevates
554 testosterone levels and protects against disease[107]. This protection, mediated by
555 microbiota-regulated sex hormones, is lost upon androgen receptor blockade[107].
556 Metabolic syndrome is also mediated by the gut microbiota in a sex-dependent
557 manner, as demonstrated by the transfer of this sex-specific effect through fecal
558 transplantation between male and female mice, with antibiotic treatment eliminating
559 these differences and highlighting the causative role of microbiota in sexual
560 dimorphism[108]. Furthermore, the microbiota regulates bone marrow mesenchymal
561 stem cells (BMMSCs) by inhibiting osteogenesis and promoting adipogenesis, as
562 shown by increased osteogenic differentiation in germ-free (GF) mice, while
563 colonization with specific-pathogen-free (SPF) microbiota restored normal BMMSC
564 proliferation, differentiation, and immunomodulatory functions[109]. The microbiota
565 regulates hematopoietic stem cell (HSC) self-renewal and differentiation under stress
566 by modulating local bone marrow iron availability through red blood cell recycling by
567 macrophages[110]. Notably, the gut microbiota modulates the expression of SAA3 in
568 colonic and adipose tissue via Toll-like receptor signaling[105]. These findings suggest
569 that the gut microbiota may influence confounding factors, such as iron availability
570 and SAA3 levels, within the tissue microenvironment, thereby affecting sex
571 dimorphism and immune cell differentiation. The SAA3-induced sex dimorphism
572 observed in previous studies may also be influenced by microbiota-driven effects on
573 bone marrow cell differentiation during early life.
574 Previous study indicates that SAA3 promotes atherosclerosis in male mice while
575 providing protective effects in female mice[103]. Jylhava et. al. suggests a potential sex-
576 dimorphism in the relationship between serum amyloid A (SAA) and early
577 atherosclerosis, as SAA levels correlated with carotid intima-media thickness (IMT)

578 in men but not in women, indicating differing underlying mechanisms of
579 atherosclerotic risk between the sexes[111]. The absence of SAA3 in female mice led to
580 a significant decrease in adipose tissue macrophage content and inflammation, while
581 similar effects were not observed in male mice[112]. Another study highlights a
582 significant sex dimorphism in the association between SAA levels and adipocyte size,
583 with pronounced correlations observed in lean and overweight women, while no such
584 associations were found in men[113]. Our results indicate there is still less aortic plaque
585 progression in female atherosclerotic *Saa3*$^{-/-}$ than in WT mice (Fig. 1). The gender
586 differences were minimal but SAA3 significantly reduced cholesterol efflux genes
587 and increased synthesis genes, particularly in female WT foamy macrophages (Fig.
588 6). SAA3-treated WT BMDMs showed downregulation of tissue repair and lipid
589 metabolism genes and upregulation of acute inflammatory and interferon-response
590 genes, aligning with *in vivo* phenotypes of Trem2^{hi} macrophages in *Saa3*$^{-/-}$ mice
591 represented the higher expression of lipid metabolism genes (Fig. 6). These results
592 suggest that SAA3 modulates inflammatory and lipid pathways in foamy
593 macrophages, which may be exacerbating atherosclerosis progression *in vivo*.
594 Notably, our study demonstrates that *Saa3* deficiency reduces aortic plaque
595 progression while increasing peripheral cholesterol levels (Figs. 1b-1e). This finding
596 aligns with previous research indicating that SAA diminishes the anti-inflammatory
597 and antioxidative capabilities of high-density lipoprotein (HDL) by binding to
598 glycoproteins from adipocytes and macrophages, thereby impairing its anti-
599 inflammatory properties[19,114]. It suggests that serum amyloid A (SAA) compromises
600 HDL functionality, which could explain the elevated cholesterol levels observed in
601 *Saa3*$^{-/-}$ mice. Despite this, *Saa3*$^{-/-}$ mice decreased aortic plaque size, indicating that
602 *Saa3* deficiency protects against atherosclerosis (Figs 1d-e).

603 The single-cell RNA sequencing (scRNA-seq) analysis of CD45+ cells from aortic
604 arches revealed significant alterations in the aortic immune cell landscape of *Saa3*$^{-/-}$
605 mice. Increased proportions of T cells, B cells, monocytes, and γδ T cells were noted,
606 while macrophages and innate lymphoid cells (ILCs) were reduced compared to WT
607 mice (Fig. 2b). This shift in immune cell composition suggests that *Saa3* deficiency
608 alters the inflammatory responses within the aortic arches, potentially contributing to
609 the observed reduction in plaque progression. *CellChat* analysis further highlighted
610 the impact of *Saa3* deficiency on intercellular communication within the aortic
611 microenvironment (Figs. 2, 3). *Saa3*$^{-/-}$ mice exhibited enhanced intercellular
612 interactions strength, particularly among γδ T cells and all other immune cell types,
613 suggesting a more reactive immune milieu. Conversely, a reduced macrophage-to-all
614 other immune cell signalings were observed, indicating a dampened inflammatory
615 response (Figure 2d-2f). These findings suggest that *Saa3* deficiency promotes a shift
616 towards a reparative and less inflammatory phenotype in these cell types, potentially
617 influencing atherosclerosis progression.
618 Compared to our previously published dataset, where we profiled single-cell sorted
619 *Cx3cr1*-derived aortic macrophages during atherosclerosis progression and
620 regression[8], we identified 11 aortic macrophage clusters, while we only identified five
621 distinct clusters with notable differences in gene expression between WT and *Saa3*$^{-/-}$
622 mice (Fig. 3a). This may be due to the difference in the platform used to capture
623 single cells between 10X Genomics and BD Rhapsody. Nonetheless, we still observed
624 that Trem2^{hi} macrophages were more abundant in *Saa3*$^{-/-}$ mice (Fig. 3b) and exhibited
625 gene expression profiles indicative of enhanced lipid metabolism and tissue repair
626 functions (Fig. 5). These macrophages may be crucial in mitigating plaque
627 progression by promoting an anti-inflammatory environment and enhancing

628 extracellular matrix production. Our findings also highlight the differential ligand-
629 receptor interactions in WT and *Saa3*$^{-/-}$ mice macrophages (Supplementary Fig. 3).
630 *Saa3* deficiency led to altered signaling dynamics, particularly in Trem2^{hi}
631 macrophages, which showed increased interactions involving *Spp1* and integrins, as
632 well as type IV collagen, suggesting enhanced adhesion and migration capabilities. In
633 contrast, chemokine-mediated communications were more prominent in WT
634 macrophages, facilitating the recruitment of inflammatory cells to atherosclerotic
635 lesions (Supplementary Fig. 3d). The observed changes in gene expression and
636 intercellular communication underscore the complex role of *Saa3* in modulating
637 Trem2^{hi} macrophage functions during atherosclerosis. *Saa3* deficiency appears to
638 shift Trem2^{hi} macrophages towards a phenotype that promotes tissue repair and
639 plaque stability (Fig. 5), which may explain the reduced plaque progression despite
640 elevated cholesterol levels.
641 In conclusion, our study reveals that *Saa3* deficiency has a dual impact on
642 atherosclerosis, reducing aortic plaque progression while increasing peripheral lipid
643 levels. The enhanced reparative and anti-inflammatory properties of macrophages in
644 *Saa3*$^{-/-}$ mice likely contribute to the observed protective effects against
645 atherosclerosis. These findings provide valuable insights into the regulatory
646 mechanisms of immune function within the aortic niche and highlight the potential of
647 targeting *Saa3* for therapeutic strategies in atherosclerosis. Further research is
648 warranted to elucidate the precise molecular pathways involved and to explore the
649 therapeutic potential of modulating *Saa3* expression in cardiovascular diseases.
650

651 **Author Contributions**

652 TYC, YZY, and JDL designed experiments and interpreted the data. TYC and YZY
653 wrote the manuscript draft, followed by JDL editing. TYC, YZY, IJL, CJL, CHY,
654 YTC, and PAC performed experiments. TYC and YZY coordinated and performed
655 the single-cell RNA-seq experiments and then analyzed single-cell RNA-seq data.

656

657 **Acknowledgments**

658 We thank the Animal Resource Center and the Consortium of Integrative Biomedical
659 Science Key Technology at National Taiwan University for their technical support.
660 Funding: This work was financially supported by the National Science and
661 Technology Council, Taiwan (110-2636-B-002-021, 111-2636-B-002-024, 112-2636-
662 B-002-015, 113-2636-B-002-009), National Taiwan University (113L894501, 113-
663 UN0066), Ministry of Education (Yushan Young Fellow Program, Featured Areas
664 Research Center Program of "Center for Advanced Computing and Imaging in
665 Biomedicine" (NTU-113L900701))

666

667

668

669 # Method

670

671 **Animals**

672 All animal procedures were approved by the National Taiwan University IACUC
673 Committee. The Saa3-knockout mice (*Saa3*$^{-/-}$; C57BL/6N-
674 Saa3tm1.1(KOMP)Vlcg/MbpMmucd) were developed by the Mutant Mouse
675 Resource & Research Centers (MMRRC). The ES cell clone 13807A-A1 was injected
676 into morulae or blastocysts to generate chimeric mice. These chimeras were then bred
677 with C57BL/6N mice, resulting in the production of heterozygous tm1 (Deletion)
678 mice. To achieve recombination at the LoxP sites, heterozygous tm1 mice were
679 crossed with a ubiquitous Cre deleter mouse line, generating tm1.1 (CRE-mediated
680 Deletion) allele mice. Notably, the archived germplasm does not carry the Cre
681 transgene. Cryo-recovery of the strain will be conducted using C57BL/6N females by
682 the MMRRC. Detailed information about the Cre-mediated deletion process can be
683 found at the following reference: Velocigene KOMP Repository, clone 13807,
684 http://velocigene.com/komp/detail/13807. The cryopreserved sperm were acquired
685 and recovered by the National Laboratory Animal Center in Taiwan. We generated
686 heterozygous *Saa3*$^{+/-}$ mice and bred them to obtain 12-week-old Wild-type C57BL/6J
687 mice wild-type (WT) and *Saa3*$^{-/-}$ littermates used for the experiments. Murine
688 atherosclerosis was induced by injecting intraperitoneally once with AAVmPCSK9
689 (ssAAV8/hAAT-mPCSK9D377Y, AAV core, Institute of Biomedical Sciences,
690 Academia Sinica, using a plasmid acquired from Addgene (Plasmid #58376) and
691 kindly provided by Dr. Mi-Hua Tao) at 5×10^{11} viral particles/mouse and fed on
692 Western diet (Research Diets, Cat# D12079Bi) for 18 weeks. All mice were housed in
693 a specific pathogen-free (SPF) environment within individually ventilated cages

694 (IVC) at a ventilation rate of 70-100 air changes per hour (ACH) under positive
695 pressure. The facility maintained a constant temperature of 22 ± 2°C and a relative
696 humidity of 55 ± 10%. A 12-hour light-dark cycle was regulated by timers (7:00 AM
697 to 7:00 PM light, 7:00 PM to 7:00 AM dark).
698

699 **Cholesterol level measurements**

700 Blood samples were collected from mice and total cholesterol levels in plasma were
701 assessed in WT and *Saa3*$^{-/-}$ mice subjected to AAVmPCSK9D377Y and fed on
702 Western Diet for 0, 4, 8, 12, and 16 weeks (n=5 mice per group). Cholesterol levels
703 were measured using a colorimetric assay (FUJIFILM/Wako, Cat# 639-50981), with
704 absorbance read at 600 nm following a 5-minute incubation at 37 °C. HDL and
705 LDL/VLDL cholesterol levels in plasma were quantified using the ab65390
706 Cholesterol Assay Kit (Abcam, Version 13a, Updated 17 April 2023), following the
707 manufacturer's protocol with adaptations for our setup. Plasma (20-30 µL) was mixed
708 with an equal volume of 2X Precipitation Buffer to separate the HDL and LDL/VLDL
709 cholesterol fractions. After adding reaction mixes, samples were incubated at 37 °C
710 for 60 minutes away from light. Absorbance was measured at 570 nm using a
711 microplate reader, and cholesterol concentrations were determined by correlating
712 absorbance readings with the standard curve. Statistically significant differences

713 between the two groups at respective time points were determined using the unpaired

714 Mann-Whitney U-test (*$p < 0.05$).

715

716 **Histology**

717 At harvesting, the aortic arch was meticulously excised from the experimental mice

718 for the subsequent single-cell isolation, and then aortic roots were embedded in OCT

719 (Catalog # NC0696746). Serial sections were performed at 6 μm on embedded aortic

720 roots and stained with Oil Red O solution (Sigma) for 10 minutes at 37°C. Intimal

721 lesions and stained areas were imaged by an inverted fluorescence microscope

722 (OLYMPUS CKX53) and quantified by ImageJ [17].

723

724 **Aortic cells flow cytometry sorting and single-cell RNA-seq library preparation**

725 The protocol for isolating aortic cells from mice is as previously described[8]. Briefly,

726 the procedure began with aorta perfusion using phosphate-buffered saline (PBS).

727 After perfusion, the aortas were stored in FACS buffer (1X HBSS, 1% BSA, 1mM

728 EDTA, 20mM HEPES, and 1mM Sodium Pyruvate). The enzymatic digestion

729 processes involved immersing the aorta in a digestion buffer containing 4U/ml

730 liberase (Roche, Cat. 54001127001), 100 ug/ml hyaluronidase (Sigma, Cat. H3506),

731 and 100 ug/ml DNase I (Sigma, Cat. DN25), followed by fine mincing. The mixture
732 was incubated at 37°C to facilitate effective digestion, with the process repeated 5-6
733 times to ensure complete tissue breakdown. After digestion, the mixture was filtered
734 through a 35μm strainer to obtain a single-cell suspension. The collected cells were
735 then stained with CD45 (Alexa Fluor 488 anti-mouse CD45, Clone: 30-F11,
736 Biolegend, Cat. 103122) and Live/Dead (L/D) Blue markers (Thermo Fisher, Cat.
737 L34962), and the CD45-positive, L/D Blue-negative cells were sorted as
738 Supplementary Figure 1 to prepare single-cell libraries.
739 Single-cell samples were labeled using the BD™ Mouse Immune Single-Cell
740 Multiplexing Kit (Cat. 633793) for each cartridge run on the BD Rhapsody Express
741 Single Cell Analysis System for single-cell capture, followed by cDNA synthesis with
742 the BD Rhapsody cDNA Kit (Cat. 633773). The mRNA Whole Transcriptome
743 Analysis (WTA) and Sample Tag libraries were prepared using the BD Rhapsody™
744 WTA Amplification Kit (Cat. 633801), according to the manufacturer's guidelines.
745 The quality and quantity of the libraries were assessed using the Agilent 4200
746 TapeStation System with Agilent High Sensitivity D1000 ScreenTape (Agilent
747 Technologies, Santa Clara, CA) and a Qubit Fluorometer with the Qubit dsDNA HS
748 Assay (Invitrogen, MA, USA). Finally, the libraries were sequenced using the
749 NovaSeq PE150 sequencer (Illumina, San Diego, CA).

750

751 **Aortic single-cell sequencing data reads alignment and analysis**

752 The fastq files generated from sequencing were processed using Seven Bridges
753 Genomics. The data were aligned to the mouse_GRCm38-PhiX-gencodevM19-
754 20181206 and demultiplexed using hashtags to separate samples. Subsequent steps
755 included filtering low-quality cells and identifying unique molecule identifiers
756 (UMIs) to produce filtered matrices, which were then utilized as inputs for further
757 analysis. The filtered matrices were analyzed using the Seurat package (v.4.3.0)[103] in
758 R (v.4.3.1). Initially, to exclude low-quality cells, we filtered out cells with
759 nFeature_RNA < 200 and percent.mt > 15, tailoring filter parameters for each sample
760 based on violin plots of RNA feature numbers and the percentage of mitochondria in
761 each cell. We used the FindVariableFeatures() function in each sample to select the
762 top 2000 genes with the highest variance using the variance variance-stabilizing
763 transformation (VST) method for downstream analysis. Next, we applied a linear
764 transformation to scale the data, ensuring equal weight to each gene expression level
765 in downstream analysis. A linear dimensional reduction (PCA) was performed, and
766 the Elbow plot was used to decide which PCs to include in the following steps. We
767 cluster cells using the Louvain algorithm (resolution = 0.5). The non-linear
768 dimensional reduction method was employed for visualizing cell clustering, such as
769 UMAP.

770 To analyze two or more single-cell datasets together, we followed the Seurat
771 integration analysis pipeline. We used the FindIntegrationAnchors() function to
772 identify anchors, followed by the IntegrateData() function to use these anchors to
773 integrate the datasets. To automatically annotate cell types, SingleR (v.2.8.0) was

774 utilized with the ImmGen database, which specifically focuses on immunological cell
775 types. To ensure the analysis targeted the immune population, contaminating cell
776 types such as fibroblasts and stromal cells were subsequently excluded. To identify
777 differentially expressed features, we employed the FindAllarkers() or FindMarkers()
778 functions to identify biomarkers for each cell cluster (min.pct = 0.25, logfc.threshold
779 = 0.25). We used visualization tools such as VlnPlot, feature plot, dotplot, and
780 heatmap to display intergroup gene expression differences. Additionally, to
781 comprehend the potential biological pathway connections of gene sets expressed by
782 each cell population and their differences between two genotypes, we conducted a
783 Gene Ontology (GO) analysis using the ClusterProfiler package (v4.8.3)[104]. This was
784 done after identifying differentially expressed genes (DEGs) in each cell population
785 compared to the cell population of another genotype. The results were visualized
786 using a Dotplot. Moreover, the analysis of intercellular communications was
787 conducted using the CellChat package (v1.6.1)[105]. This approach allowed us to
788 understand the roles played by each cell group in signal transduction pathways and
789 compare the differences in cellular signaling among cell groups under different
790 genotypes.

791

792 **Bone marrow-derived macrophages (BMDMs) culture**

793 Bone marrow cells harvested from C57BL/6J mice were cultured in RPMI 1640
794 medium supplemented with 10% heat-inactivated fetal bovine serum (FBS), 1%
795 penicillin/streptomycin/amphotericin B (P/S/A), and 20 ng/mL macrophage colony-
796 stimulating factor (M-CSF). On day 3, the medium was replaced with 10 mL fresh
797 medium. On day 5, an additional 2 mL of medium was added. After seven days of
798 culture, adherent macrophages were detached using Accutase and treated with 100

799 ng/mL SAA3 protein. The cell suspension was adjusted to a density of 5×10^6
800 cells/mL, seeded into a 48-well plate, and cultured for 24 hours.
801
802 **Real-time RT-PCR**
803 Total RNA was extracted from BMDMs using TRIzol™ Reagent, and cDNA was
804 synthesized using SuperScript™ IV Reverse Transcriptase. Real-time RT-PCR was
805 performed with TaqMan™ Fast Advanced Master Mix on a CFX Connect Real-Time
806 PCR Detection System. The assays utilized the following TaqMan probes: *Gapdh*
807 (Mm99999915_g1), *Saa1* (Mm00656927_g1), *Saa2* (Mm04208126_mH), *Saa3*
808 (Mm00441203_m1), *Il-1β* (Mm00434228_m1), and *Tnf* (Mm00443258_m1).
809 Additionally, real-time RT-PCR was also conducted using iTaq™ Universal SYBR®
810 Green Supermix with primers targeting *Abca1*, *Abcg1*, *Hmgcr*, and *Cyp51*. The fold
811 change in each target mRNA was determined by normalizing its expression level to
812 *Gapdh* within the same sample. Relative gene expression was calculated using the
813 comparative method ($2^{-\Delta\Delta CT}$).
814
815 **BMDM single-cell RNA library preparation and sequencing**
816 BMDMs were fixed and permeabilized according to the Evercode™ Fixation v2
817 protocol (Parse Biosciences). The split-pool barcoding process, following the
818 Evercode™ WT v2 protocol, consisted of three rounds. In Round 1, cells were
819 distributed into wells, and sample-specific barcodes were applied to the fixed cells
820 using an in-cell reverse transcription (RT) reaction. Cells from all wells were then
821 pooled together. In Round 2, cells were redistributed across a plate, and an in-cell
822 ligation was performed to append the second barcode. The cells from each well were
823 again pooled together. In Round 3, cells were split across a plate, and a third barcode

824 was appended with another in-cell ligation. After pooling cells from each well, the
825 pooled cells were divided across multiple sublibraries. The cells were then lysed, and
826 the library was fragmented, end-repaired, and went through A-tailing followed by the
827 ligation of the sequencing adaptor. The library was then labeled with a fourth
828 sublibrary-specific barcode. The quality of dsDNA libraries was analyzed using the
829 High Sensitivity D5000 ScreenTape Kit (Agilent) and concentrations were assessed
830 with the Qubit dsDNA HS Kit (Thermo Fisher Scientific). Libraries were sequenced
831 on a NovaSeq X Plus (Illumina) with 10% PhiX.
832
833 **BMDM single-cell RNA data processing**
834 The sequencing data was demultiplexed and mapped to database (mm10, GRCm38)
835 with the commercial pipeline (ParseBiosciences-Pipeline.v1.2.1). The sequence reads
836 from different samples was then distributed based on different Round 1 barcode with
837 R(v4.4.2). To exclude low-quality cells, we filtered cells with nFeature_RNA > 200,
838 nFeature_RNA < 2000, and percent.mt < 45, adjusting the filter parameters for each
839 sample based on violin plots of RNA feature counts and mitochondrial percentages
840 per cell. The FindVariableFeatures() function was used to select the top 2000 genes
841 with the highest variance, applying the variance-stabilizing transformation (VST)
842 method for downstream analysis. The data were then scaled using a linear
843 transformation to ensure equal weighting of gene expression levels in subsequent
844 analyses. Principal component analysis (PCA) was performed for linear dimensional
845 reduction, and the Elbow plot was used to determine the number of principal
846 components (PCs) to retain. Cell clustering was conducted using the Louvain
847 algorithm with a resolution of 0.5. For visualization, we applied the non-linear
848 dimensional reduction method UMAP. For integrating two or more single-cell
849 datasets, we followed the Seurat integration analysis pipeline. The IntegrateLayers()

function with the CCAIntegration method was used for dataset integration, followed by the JoinLayers() function to merge the layers. Cell types were annotated automatically using SingleR (v2.8.0) with the ImmGen database, which specializes in immunological cell types. Contaminating cell types, such as fibroblasts, were excluded to ensure the analysis focused on the immune population. To identify potential biological pathway connections and differences following SAA3 protein treatment, we performed Gene Ontology (GO) analysis using the ClusterProfiler package (v4.10.1) on differentially expressed genes (DEGs) from BMDMs under different conditions. Results were visualized using DotPlot representations.

Data and code availability

Raw sequence data from single-cell RNA sequencing experiments are deposited in the NCBI Sequence Read Archive under BioProject accession number PRJNA1129034 and gene expression omnibus (GEO) accession number GSE270922. All processing was performed in R and analysis scripts can be found on Github at (https://github.com/JDLinLab/Saa3KO-Arch-scRNAseq-pepline-)

872 **Figure legend**

873 **Fig. 1 Effects of *Saa3* deletion on peripheral lipid profiles and aortic plaque**

874 **progression during atherosclerosis.**

875 **(a)** Schematic of an experimental model for the time points of plasma collections and

876 single-cell RNA sequencing (scRNA-seq) on aortic immune cells. C57BL/6 wild-type

877 (WT) and *Saa3*$^{-/-}$ mice were injected with AAVmPCSK9 and fed with the Western

878 diet for 18 weeks. Then aortic arches were digested to single-cell suspensions and

879 FACS-sorted aortic CD45+ cells were subjected to scRNA-seq on the BD Rhapsody

880 platform from WT and *Saa3*$^{-/-}$ mice.

881 **(b)** Plasma total cholesterol levels in WT and *Saa3*$^{-/-}$ mice subjected with

882 ssAAV8/hAAT-mPCSK9 and fed with the Western diet for 0, 4, 8, 12, and 16 weeks.

883 **(c)** Measurement of high-density lipoprotein (HDL) cholesterol levels and low-

884 density lipoprotein (LDL) cholesterol levels in plasma from WT and *Saa3*$^{-/-}$ mice over

885 a period of 0, 2, 4, 8, 12, and 16 weeks.

886 **(d)** Representative Oil Red O staining of aortic root sections in WT and *Saa3*$^{-/-}$ mice

887 at 18 weeks post Western diet. Scale bar: 100 μm.

888 **(e)** As in (d), quantification of the lesion area of aortic root sections stained with Oil

889 Red O.

890 All data are presented as mean ± SEM; Statistically significant differences between

891 the two groups at respective time points were denoted by asterisks (*$p < 0.05$),

892 determined using an unpaired Mann-Whitney U-test. Each symbol represents an

893 individual mouse; WT mice (n=5), *Saa3*$^{-/-}$ mice (n=5).

894

895 **Fig. 2 *Saa3* deficiency alters immune intercellular communication in aortic**

896 **arches during atherosclerosis progression.**

897 **(a)** UMAP visualization compares the distribution of cell types in aortic arches

898 between WT and *Saa3*$^{-/-}$ mice. Unbiased cell annotations against the IMMGEN

899 database are colored and labeled accordingly on the plot.

900 **(b)** Cell type composition by percentages of WT and *Saa3*$^{-/-}$ mice (blue, WT; red,

901 *Saa3*$^{-/-}$) in total sorted CD45+ cells.

902 **(c)** Heatmap of top 5 marker genes of each cell type in aortic arches from WT and

903 *Saa3*$^{-/-}$ mice. The selection of these top marker genes was based on the results of a

904 Wilcoxon test for differential expression.

905 **(d)** Bar plots show the number (left) and strength (right) of inferred interactions of

906 intercellular communication networks in aortic arches from WT and *Saa3*$^{-/-}$ mice.

907 **(e)** Heatmap visualization of intercellular communication networks in aortic arches

908 from WT and *Saa3*$^{-/-}$ mice. The red and blue colors represent increased or

909 decreased signaling in the aortic arches of *Saa3*$^{-/-}$ mice compared to the WT mice. The
910 top-colored bar plot represents the sum of the columns of values (incoming signaling),
911 and the right-colored bar plot represents the sum of a row of values (outgoing
912 signaling).
913 **(e)** Volcano plot illustrating differential gene expression in total macrophages within
914 aortic arches of *Saa3*$^{-/-}$ versus WT mice. The x-axis displays the $\log_2$ fold change,
915 while the y-axis shows the -Log_{10} *p*-value. Grey dots denote genes without significant
916 differences, green dots indicate genes with significant fold changes, and red dots mark
917 genes significant in both fold change and *p*-value. The dashed vertical lines represent
918 the fold change boundaries, and the dashed horizontal line demonstrates the p-value
919 significance threshold.
920 **(g)** Top 10 biological processes enriched in total macrophages within the aortic arches
921 of WT mice compared to *Saa3*$^{-/-}$ mice (upper panel) or *Saa3*$^{-/-}$ mice compared to wild-
922 type mice (lower panel). Enrichment analysis utilized GO pathways to identify
923 significant biological processes. The gene ratio is plotted along the x-axis, and the
924 enriched biological processes are listed on the y-axis. A color gradient has been
925 applied to indicate the -$\log_{10}$ adjusted *p*-value (p.adjust) of each term, with the size of
926 each point reflecting the number of genes associated with the respective pathway.
927

928 **Fig. 3 Delineation of macrophage sub-cluster in aortic arches between WT and**

929 ***Saa3*$^{-/-}$ mice during atherosclerosis progression.**

930 **(a)** UMAP plots show the sub-clusters of macrophages (Mφ) in aortic arches between

931 WT (left) and *Saa3*$^{-/-}$ (right) mice. Macrophages are delineated based on their gene

932 expression profiles: CD74^{hi}MHCII^{hi} Mφ in navy blue, Folr2^{hi} Mφ in red,

933 Retnla^{hi}Ear2^{hi} Mφ in green, Trem2^{hi} Mφ in sky blue, and Apbb2^{hi} Mφ in pink.

934 **(b)** The bar graph displays the percentage composition of various macrophage

935 subpopulations within total macrophages from WT and *Saa3*$^{-/-}$ mice. Different colors

936 represent distinct macrophage subpopulations as indicated in **(a)**.

937 **(c)** Dot plot representing the expression profiles of five sub-macrophage populations.

938 The x-axis lists genes with differential expression, while the y-axis indicates the sub-

939 macrophage clusters.

940 **(d)** Dot plots show the expression profiles of macrophage markers involved in

941 pathways of chemokine, IFN (interferon), inflammatory, and type II responses across

942 sub-macrophage clusters. For **(c)** and **(d)**, the size of each dot corresponds to the

943 percentage of the indicated cell cluster expressing a particular gene marker, and the

944 color intensity signifies the mean expression level within that cell cluster.

945 **(e)** Bar plots show the number (left) and strength (right) of inferred intercellular

946 communication networks in total aortic macrophages from WT and *Saa3*$^{-/-}$ mice.

947 **(f)** Heatmap visualization of overall signaling patterns in aortic macrophages of WT

948 and *Saa3*$^{-/-}$ mice. The top-colored bar plot represents the sum of each column of

949 values (signaling the strength of overall pathways) across sub-clusters. The gradient

950 blue colored bar represents the relative strength of the indicated pathway.

951 **(g)** The bar graph displays the relative information flow of various signaling

952 molecules in aortic macrophages of WT and *Saa3*$^{-/-}$ mice. Blue bars indicate higher

953 relative information flow in WT macrophages, while red bars indicate higher

954 information flow in *Saa3*$^{-/-}$ macrophages.

955

956 **Fig. 4 *Saa3* deficient impacts gene expression profiles of aortic macrophages**

957 **(a)-(d)** Volcano plot illustrating differential gene expression in four sub-macrophage

958 populations (CD74^{hi} MHCII^{hi} , Folr2^{hi}, Retnla^{hi} Ear2^{hi}, and Apbb2^{hi} macrophage(Mφ))

959 within aortic arches of WT versus *Saa3*$^{-/-}$ mice. The x-axis displays the $\log_2$ fold

960 change, while the y-axis shows the -Log_{10} p-value. Grey dots denote genes without

961 significant differences, green dots indicate genes with significant fold changes, and

962 red dots mark genes significant in both fold change and *p*-value. The dashed vertical

963 lines represent the fold change boundaries, and the dashed horizontal line

964 demonstrates the *p*-value significance threshold.

965 **(e)-(h)** The bubble plot presents the GO enrichment analysis for CD74^{hi} MHCII^{hi} ,

966 Folr2^{hi}, Retnla^{hi} Ear2^{hi}, and Apbb2^{hi} aortic macrophage (Mφ) from WT and *Saa3*$^{-/-}$

967 mice. The x-axis represents the GeneRatio. The y-axis lists the enriched GO terms.

968 Bubble size corresponds to the count of DEGs associated with each GO term. The

969 color gradient from blue to red represents the -$\log_{10}$ (adjusted *p*-value) of the

970 enrichment.

971

972 **Fig. 5 Aortic Trem2^{hi} macrophages in *Saa3*$^{-/-}$ mice express more lipid metabolism**

973 **and tissue repair-associated genes.**

974 **(a)** Volcano plot illustrating differential gene expression in aortic Trem2^{hi}

975 macrophage (Mφ) population of *Saa3*$^{-/-}$ versus WT mice.

976 **(b)** The bubble plot presents the GO enrichment analysis for Trem2^{hi} Mφ from WT

977 versus *Saa3*$^{-/-}$ (upper panel) or *Saa3*$^{-/-}$ versus WT (lower panel) mice.

978 **(c)** Violin plots depicting the expression levels of tissue repair-associated genes in

979 Trem2^{hi} Mφ from WT and *Saa3*$^{-/-}$ mice aortas. Each plot indicates the gene expression

980 level for *Gpnmb*, *Fabp5*, *Lpl*, *Lgals3*, *Spp1*, *Cd36*, and *Pparg*, with blue representing

981 WT and red for *Saa3*$^{-/-}$ group. The central white bar denotes the median expression

982 level, while the thick bar within the violins indicates the interquartile range. The

983 width of the violins reflects the density of data points at different expression levels.

984 **(d)** The circular diagram illustrates the GDF signaling pathway networks in aortic
985 macrophage subpopulations from WT (left) and *Saa3*$^{-/-}$ (right) mice. Each segment of
986 the circle represents a different macrophage subpopulation. The connections between
987 segments indicate interactions and signaling pathways shared among these
988 subpopulations.
989 **(e)** Heatmap representation of the inferred GDF signaling pathway network across
990 five sub-populations of aortic macrophages. Each column represents a specific
991 macrophage sub-population, while each row corresponds to the role of the population
992 in the signaling pathway as a sender, receiver, mediator, or influencer.
993
994 **Figure 6. SAA3 modulates cholesterol metabolism, inflammatory gene**
995 **expression, and immune response pathways in macrophages under steady-state**
996 **condition or during foamy macrophage differentiation.**
997 **(a)** Schematic overview of the experimental design. Bone marrow cells were isolated
998 from WT and *Saa3*$^{-/-}$ mice. Then cultured and differentiated into bone marrow-
999 derived macrophages (BMDMs), followed by treatment with soluble cholesterol to
1000 induce foamy macrophages or recombinant SAA3 protein. Downstream analyses
1001 included real-time PCR and single-cell RNA sequencing (scRNA-seq) using Parse
1002 Evercode™.
1003 **(b-c)** As treatment conditions in **(a)**, Real-time PCR analysis of genes involved in
1004 inflammatory cytokines (*Il1b*, *Tnf*) and cholesterol metabolism (*Abca1*, *Abcg1*,
1005 *Cyp51*, *Hmgcr*) and under various treatment conditions. Data are represented as

relative gene expression normalized to the control group, with significant differences marked by asterisks (*$p < 0.05$, **$p < 0.01$, ***$p < 0.001$). The symbols represent the following comparisons: **φ** indicates SAA3-treated male WT BMDMs versus male WT BMDMs cultured in media alone, **§** indicates SAA3-treated female WT BMDMs versus female WT BMDMs cultured in media alone, # indicates SAA3-treated male WT BMDMs in the presence of soluble cholesterol versus male WT BMDMs in soluble cholesterol media alone, and † indicates SAA3-treated female WT BMDMs in the presence of soluble cholesterol versus female WT BMDMs in soluble cholesterol media alone. The number of symbols denotes the level of statistical significance, where one symbol indicates $p < 0.05$, two symbols indicate $p < 0.01$, and three symbols indicate $p < 0.001$.

(d-f) scRNA-seq analysis of WT BMDMs treated with media alone or SAA3 protein.

(d-e) Dot plots show average expression (color intensity) and the percentage of cells expressing key genes (dot size) related to tissue repair, lipid metabolism, and inflammatory pathways.

(f) Gene Ontology (GO) enrichment analysis of pathways upregulated in SAA3-treated BMDMs compared to controls. Size of dots represents the gene ratio, and color intensity represents statistical significance ($-\log_{10}$ (adjusted p-value)). Statistical significance was determined using ANOVA or t-tests where appropriate.

1029

1030 ## Supplementary Figure Legends

1031 **Supplementary Fig. 1 Sorting strategy of aortic CD45+ cells.**

1032 Flow cytometry analysis was performed for cell sorting to isolate CD45+ immune
1033 cells from aortic arches stained for CD45 Alexa 488 and Live/Dead Blue. The top left
1034 plot shows forward scatter (FSC-A) versus side scatter (SSC-A), differentiating cells
1035 based on size and granularity, with a population gated as P1. The top right plot
1036 presents FSC-A versus FSC-H, with the discrimination gate P2 to exclude cell
1037 aggregates. The bottom left plot displays SSC-A against the Live/Dead Blue, with live
1038 cells gated as P7. The bottom right plot demonstrates SSC-A against the fluorescence
1039 intensity of CD45 Alexa-488, with the CD45+ population gated as P8. The CD45+
1040 cells were sorted from P8 gated population.

1041

1042 **Supplementary Fig. 2 Heatmap of top 10 gene markers and GO enrichment**
1043 **analysis of five aortic macrophage sub-cluster.**

1044 **(a)** Heatmap of top 10 marker genes of each sub-macrophage population in aortic
1045 arches from WT and *Saa3*$^{-/-}$ mice. The selection of these top marker genes was based
1046 on the results of a Wilcoxon test for differential expression.

1047 **(b)** Gene Ontology (GO) enrichment analysis of biological pathways in 5 sub-
1048 populations of aortic macrophage (Mφ), using differentially expressed genes (DEGs)
1049 identified when comparing one of specific Mφ sub-population against the rest of all
1050 other Mφ sub-populations. It can represent the functional characteristics of each Mφ
1051 sub-population.

1052

1053 **Supplementary Fig. 3 Comparison of ligand-receptor pair differences across five**
1054 **sub-macrophage populations between WT and *Saa3*$^{-/-}$ mice.**
1055 The bubble plot illustrating the protein-protein interaction probabilities between
1056 various ligand-receptor pairs across **(a)** CD74^{hi} MHCII^{hi} macrophage (Mφ), **(b)**
1057 Folr2^{hi} Mφ, **(c)** Retnla^{hi} Ear2^{hi} Mφ, **(d)** Trem2^{hi} Mφ, and **(e)** Apbb2^{hi} Mφ between WT
1058 and *Saa3*$^{-/-}$ mice. The x-axis categorizes the conditions under which the interactions
1059 were assessed. The y-axis lists the ligand-receptor pairs. Each bubble's color
1060 corresponds to the communication probability, with a gradient from minimum (blue)
1061 to maximum (red). The communication probability can be seen as a numerical value
1062 representing how strong or likely this interaction is between specific cell types. The
1063 size of each bubble represents the *p*-value of the interaction.
1064
1065 **Supplementary Fig. 4 Comparison of differences in the expression level of**
1066 **cholesterol efflux and lipid metabolism genes from Trem2^{hi} macrophages**
1067 **between WT and *Saa3*$^{-/-}$ mice.**
1068 Differential gene expression in aortic Trem2^{hi} macrophages (Mφ) from WT and *Saa3*$^{-}$
1069 $^{/-}$ mice. Violin plots illustrate the distribution of expression levels for genes involved
1070 in cholesterol efflux and lipid metabolism in Trem2^{hi} macrophages. Blue represents
1071 WT macrophages, while red indicates *Saa3*$^{-/-}$ macrophages.
1072
1073
1074
1075
1076

1077

1078 **Reference**

1079 1 Benjamin, E. J. *et al.* Heart Disease and Stroke Statistics-2019 Update: A Report
1080 From the American Heart Association. *Circulation* **139**, e56-e528 (2019).
1081 https://doi.org/10.1161/CIR.0000000000000659

1082 2 Malekmohammad, K., Bezsonov, E. E. & Rafieian-Kopaei, M. Role of Lipid
1083 Accumulation and Inflammation in Atherosclerosis: Focus on Molecular and
1084 Cellular Mechanisms. *Front Cardiovasc Med* **8**, 707529 (2021).
1085 https://doi.org/10.3389/fcvm.2021.707529

1086 3 Libby, P. *et al.* Atherosclerosis. *Nat Rev Dis Primers* **5**, 56 (2019).
1087 https://doi.org/10.1038/s41572-019-0106-z

1088 4 Steinl, D. C. & Kaufmann, B. A. Ultrasound imaging for risk assessment in
1089 atherosclerosis. *Int J Mol Sci* **16**, 9749-9769 (2015).
1090 https://doi.org/10.3390/ijms16059749

1091 5 Sekalska, B. [Aortic expression of monocyte chemotactic protein-1 (MCP-1)
1092 gene in rabbits with experimental atherosclerosis]. *Ann Acad Med Stetin* **49**, 79-
1093 90 (2003).

1094 6 Zhang, Y. *et al.* Oxidized high-density lipoprotein promotes CD36
1095 palmitoylation and increases lipid uptake in macrophages. *J Biol Chem* **298**,
1096 102000 (2022). https://doi.org/10.1016/j.jbc.2022.102000

1097 7 Javadifar, A. *et al.* Foam Cells as Therapeutic Targets in Atherosclerosis with a
1098 Focus on the Regulatory Roles of Non-Coding RNAs. *Int J Mol Sci* **22** (2021).
1099 https://doi.org/10.3390/ijms22052529

1100 8 Lin, J. D. *et al.* Single-cell analysis of fate-mapped macrophages reveals
1101 heterogeneity, including stem-like properties, during atherosclerosis
1102 progression and regression. *JCI Insight* **4** (2019).
1103 https://doi.org/10.1172/jci.insight.124574

1104 9 Zhang, K. *et al.* TREM2(hi) resident macrophages protect the septic heart by
1105 maintaining cardiomyocyte homeostasis. *Nat Metab* **5**, 129-146 (2023).
1106 https://doi.org/10.1038/s42255-022-00715-5

1107 10 Jung, S. H. *et al.* Spatiotemporal dynamics of macrophage heterogeneity and a
1108 potential function of Trem2(hi) macrophages in infarcted hearts. *Nat Commun*
1109 **13**, 4580 (2022). https://doi.org/10.1038/s41467-022-32284-2

1110 11 Reigstad, C. S., Lunden, G. O., Felin, J. & Backhed, F. Regulation of serum
1111 amyloid A3 (SAA3) in mouse colonic epithelium and adipose tissue by the
1112 intestinal microbiota. *PLoS One* **4**, e5842 (2009).
1113 https://doi.org/10.1371/journal.pone.0005842

1114 12 Dong, Z. *et al.* Serum amyloid A directly accelerates the progression of
1115 atherosclerosis in apolipoprotein E-deficient mice. *Mol Med* **17**, 1357-1364
1116 (2011). https://doi.org/10.2119/molmed.2011.00186

1117 13 Meek, R. L., Eriksen, N. & Benditt, E. P. Murine serum amyloid A3 is a high
1118 density apolipoprotein and is secreted by macrophages. *Proc Natl Acad Sci U S*
1119 *A* **89**, 7949-7952 (1992). https://doi.org/10.1073/pnas.89.17.7949

1120 14 Sanada, Y. *et al.* Serum Amyloid A3 Gene Expression in Adipocytes is an
1121 Indicator of the Interaction with Macrophages. *Sci Rep* **6**, 38697 (2016).
1122 https://doi.org/10.1038/srep38697

1123 15 Hadrup, N. *et al.* Acute Phase Response as a Biological Mechanism-of-Action
1124 of (Nano)particle-Induced Cardiovascular Disease. *Small* **16**, e1907476 (2020).
1125 https://doi.org/10.1002/smll.201907476

1126 16 Thompson, J. C. *et al.* Serum amyloid A3 is pro-atherogenic. *Atherosclerosis*
1127 **268**, 32-35 (2018). https://doi.org/10.1016/j.atherosclerosis.2017.11.011

1128 17 Keeter, W. C., Carter, N. M., Nadler, J. L. & Galkina, E. V. The AAV-PCSK9
1129 murine model of atherosclerosis and metabolic dysfunction. *Eur Heart J Open*
1130 **2**, oeac028 (2022). https://doi.org/10.1093/ehjopen/oeac028

1131 18 Peled, M. *et al.* A wild-type mouse-based model for the regression of
1132 inflammation in atherosclerosis. *PLoS One* **12**, e0173975 (2017).
1133 https://doi.org/10.1371/journal.pone.0173975

1134 19 Han, C. Y. *et al.* Serum amyloid A-containing HDL binds adipocyte-derived
1135 versican and macrophage-derived biglycan, reducing its antiinflammatory
1136 properties. *JCI Insight* **5** (2020). https://doi.org/10.1172/jci.insight.142635

1137 20 Holmes, N. CD45: all is not yet crystal clear. *Immunology* **117**, 145-155 (2006).
1138 https://doi.org/10.1111/j.1365-2567.2005.02265.x

1139 21 Haudek, S. B. *et al.* Bone marrow-derived fibroblast precursors mediate
1140 ischemic cardiomyopathy in mice. *Proc Natl Acad Sci U S A* **103**, 18284-18289
1141 (2006). https://doi.org/10.1073/pnas.0608799103

1142 22 Stuart, T. *et al.* Comprehensive Integration of Single-Cell Data. *Cell* **177**, 1888-
1143 1902 e1821 (2019). https://doi.org/10.1016/j.cell.2019.05.031

1144 23 Aran, D. *et al.* Reference-based analysis of lung single-cell sequencing reveals
1145 a transitional profibrotic macrophage. *Nat Immunol* **20**, 163-172 (2019).
1146 https://doi.org/10.1038/s41590-018-0276-y

1147 24 Xu, B. *et al.* The Biological Functions and Regulatory Mechanisms of Fatty
1148 Acid Binding Protein 5 in Various Diseases. *Front Cell Dev Biol* **10**, 857919
1149 (2022). https://doi.org/10.3389/fcell.2022.857919

1150 25 Nickl, B., Qadri, F. & Bader, M. Anti-inflammatory role of Gpnmb in adipose
1151 tissue of mice. *Sci Rep* **11**, 19614 (2021). https://doi.org/10.1038/s41598-021-
1152 99090-6

1153 26 Ding, C. *et al.* The Teleost CXCL13-CXCR5 Axis Induces Inflammatory
1154 Cytokine Expression through the Akt-NF-kappaB, p38-AP-1, and p38-NF-
1155 kappaB Pathways. *J Immunol* **212**, 317-334 (2024).
1156 https://doi.org/10.4049/jimmunol.2300237

1157 27 Han, J. H. *et al.* Association of CXCL10 and CXCL13 levels with disease
1158 activity and cutaneous manifestation in active adult-onset Still's disease.
1159 *Arthritis Res Ther* **17**, 260 (2015). https://doi.org/10.1186/s13075-015-0773-4

1160 28 Kiss, M. G. *et al.* Cell-autonomous regulation of complement C3 by factor H
1161 limits macrophage efferocytosis and exacerbates atherosclerosis. *Immunity* **56**,
1162 1809-1824 e1810 (2023). https://doi.org/10.1016/j.immuni.2023.06.026

1163 29 Suzuki, M. *et al.* Cholesterol accumulation regulates expression of macrophage
1164 proteins implicated in proteolysis and complement activation. *Arterioscler*
1165 *Thromb Vasc Biol* **32**, 2910-2918 (2012).
1166 https://doi.org/10.1161/ATVBAHA.112.300383

1167 30 Wu, T. *et al.* clusterProfiler 4.0: A universal enrichment tool for interpreting
1168 omics data. *Innovation (Camb)* **2**, 100141 (2021).
1169 https://doi.org/10.1016/j.xinn.2021.100141

1170 31 Hou, P. *et al.* Macrophage polarization and metabolism in atherosclerosis. *Cell*
1171 *Death Dis* **14**, 691 (2023). https://doi.org/10.1038/s41419-023-06206-z

1172 32 Cochain, C. *et al.* Single-Cell RNA-Seq Reveals the Transcriptional Landscape
1173 and Heterogeneity of Aortic Macrophages in Murine Atherosclerosis. *Circ Res*
1174 **122**, 1661-1674 (2018). https://doi.org/10.1161/CIRCRESAHA.117.312509

1175 33 Nalio Ramos, R. *et al.* Tissue-resident FOLR2(+) macrophages associate with
1176 CD8(+) T cell infiltration in human breast cancer. *Cell* **185**, 1189-1207 e1125
1177 (2022). https://doi.org/10.1016/j.cell.2022.02.021

1178 34 Ensan, S. *et al.* Self-renewing resident arterial macrophages arise from
1179 embryonic CX3CR1(+) precursors and circulating monocytes immediately after
1180 birth. *Nat Immunol* **17**, 159-168 (2016). https://doi.org/10.1038/ni.3343

1181 35 Beckers, C. M. L. *et al.* Cre/lox Studies Identify Resident Macrophages as the
1182 Major Source of Circulating Coagulation Factor XIII-A. *Arterioscler Thromb*
1183 *Vasc Biol* **37**, 1494-1502 (2017).
1184 https://doi.org/10.1161/ATVBAHA.117.309271

1185 36 Sanin, D. E. *et al.* A common framework of monocyte-derived macrophage
1186 activation. *Sci Immunol* **7**, eabl7482 (2022).
1187 https://doi.org/10.1126/sciimmunol.abl7482

1188 37 Loke, P. & Lin, J. D. Redefining inflammatory macrophage phenotypes across
1189 stages and tissues by single-cell transcriptomics. *Sci Immunol* **7**, eabo4652
1190 (2022). https://doi.org/10.1126/sciimmunol.abo4652

1191 38 Cochain, C. *et al.* Single-Cell RNA-Seq Reveals the Transcriptional Landscape
1192 and Heterogeneity of Aortic Macrophages in Murine Atherosclerosis. *Circ Res*
1193 **122**, 1661-1674 (2018). https://doi.org/CIRCRESAHA.117.312509 [pii]

1194 10.1161/CIRCRESAHA.117.312509

1195 39 Muller, A. *et al.* Imaging atherosclerotic plaque inflammation via folate receptor
1196 targeting using a novel 18F-folate radiotracer. *Mol Imaging* **13**, 1-11 (2014).

1197 40 Kim, K. *et al.* Transcriptome Analysis Reveals Nonfoamy Rather Than Foamy
1198 Plaque Macrophages Are Proinflammatory in Atherosclerotic Murine Models.
1199 *Circ Res* **123**, 1127-1142 (2018).
1200 https://doi.org/10.1161/CIRCRESAHA.118.312804

1201 41 Qi, J. *et al.* Single-cell and spatial analysis reveal interaction of FAP(+)
1202 fibroblasts and SPP1(+) macrophages in colorectal cancer. *Nat Commun* **13**,
1203 1742 (2022). https://doi.org/10.1038/s41467-022-29366-6

1204 42 Hoeft, K. *et al.* Platelet-instructed SPP1(+) macrophages drive myofibroblast
1205 activation in fibrosis in a CXCL4-dependent manner. *Cell Rep* **42**, 112131
1206 (2023). https://doi.org/10.1016/j.celrep.2023.112131

1207 43 Saade, M., Araujo de Souza, G., Scavone, C. & Kinoshita, P. F. The Role of
1208 GPNMB in Inflammation. *Front Immunol* **12**, 674739 (2021).
1209 https://doi.org/10.3389/fimmu.2021.674739

1210 44 Kumari, A., Kristensen, K. K., Ploug, M. & Winther, A. L. The Importance of
1211 Lipoprotein Lipase Regulation in Atherosclerosis. *Biomedicines* **9** (2021).

1212 https://doi.org/10.3390/biomedicines9070782

1213 45 Wang, X. & Khalil, R. A. Matrix Metalloproteinases, Vascular Remodeling, and
1214 Vascular Disease. *Adv Pharmacol* **81**, 241-330 (2018).
1215 https://doi.org/10.1016/bs.apha.2017.08.002

1216 46 Zou, Y. *et al.* Nrf2 is essential for timely M phase entry of replicating
1217 hepatocytes during liver regeneration. *Am J Physiol Gastrointest Liver Physiol*
1218 **308**, G262-268 (2015). https://doi.org/10.1152/ajpgi.00332.2014

1219 47 Buechler, C. *et al.* Regulation of scavenger receptor CD163 expression in
1220 human monocytes and macrophages by pro- and antiinflammatory stimuli. *J*
1221 *Leukoc Biol* **67**, 97-103 (2000).

1222 48 Martinez, F. O. & Gordon, S. The M1 and M2 paradigm of macrophage
1223 activation: time for reassessment. *F1000Prime Rep* **6**, 13 (2014).
1224 https://doi.org/10.12703/P6-13

1225 49 Gudgeon, J., Marin-Rubio, J. L. & Trost, M. The role of macrophage scavenger
1226 receptor 1 (MSR1) in inflammatory disorders and cancer. *Front Immunol* **13**,
1227 1012002 (2022). https://doi.org/10.3389/fimmu.2022.1012002

1228 50 Zhao, S. J. *et al.* Macrophage MSR1 promotes BMSC osteogenic differentiation
1229 and M2-like polarization by activating PI3K/AKT/GSK3beta/beta-catenin
1230 pathway. *Theranostics* **10**, 17-35 (2020). https://doi.org/10.7150/thno.36930

1231 51 Kurilenko, N., Fatkhullina, A. R., Mazitova, A. & Koltsova, E. K. Act Locally,
1232 Act Globally-Microbiota, Barriers, and Cytokines in Atherosclerosis. *Cells* **10**
1233 (2021). https://doi.org/10.3390/cells10020348

1234 52 Chen, H. J., Tas, S. W. & de Winther, M. P. J. Type-I interferons in
1235 atherosclerosis. *J Exp Med* **217** (2020). https://doi.org/10.1084/jem.20190459

1236 53 Edsfeldt, A. *et al.* Interferon regulatory factor-5-dependent CD11c+
1237 macrophages contribute to the formation of rupture-prone atherosclerotic
1238 plaques. *Eur Heart J* **43**, 1864-1877 (2022).
1239 https://doi.org/10.1093/eurheartj/ehab920

1240 54 Stein, E. V., Miller, T. W., Ivins-O'Keefe, K., Kaur, S. & Roberts, D. D. Secreted
1241 Thrombospondin-1 Regulates Macrophage Interleukin-1beta Production and
1242 Activation through CD47. *Sci Rep* **6**, 19684 (2016).
1243 https://doi.org/10.1038/srep19684

1244 55 Tian, Z. *et al.* ANGPTL2 activity in cardiac pathologies accelerates heart failure
1245 by perturbing cardiac function and energy metabolism. *Nat Commun* **7**, 13016

1246 (2016). https://doi.org/10.1038/ncomms13016

1247 56 Horio, E. *et al.* Role of endothelial cell-derived angptl2 in vascular
1248 inflammation leading to endothelial dysfunction and atherosclerosis
1249 progression. *Arterioscler Thromb Vasc Biol* **34**, 790-800 (2014).
1250 https://doi.org/10.1161/ATVBAHA.113.303116

1251 57 Li, L. *et al.* Endothelial Basement Membrane Laminins as an Environmental
1252 Cue in Monocyte Differentiation to Macrophages. *Front Immunol* **11**, 584229
1253 (2020). https://doi.org/10.3389/fimmu.2020.584229

1254 58 Wang, J. & Liu, H. The Roles of Junctional Adhesion Molecules (JAMs) in Cell
1255 Migration. *Front Cell Dev Biol* **10**, 843671 (2022).
1256 https://doi.org/10.3389/fcell.2022.843671

1257 59 Mishra, B. H. *et al.* Modular genome-wide gene expression architecture shared
1258 by early traits of osteoporosis and atherosclerosis in the Young Finns Study. *Sci*
1259 *Rep* **11**, 7111 (2021). https://doi.org/10.1038/s41598-021-86536-0

1260 60 Zhang, Y. *et al.* Loss of CD226 protects apolipoprotein E-deficient mice from
1261 diet-induced atherosclerosis. *Biochim Biophys Acta Mol Basis Dis* **1868**,
1262 166452 (2022). https://doi.org/10.1016/j.bbadis.2022.166452

1263 61 Zhang, M. *et al.* Macrophage-specific deletion of Notch-1 induced M2 anti-
1264 inflammatory effect in atherosclerosis via activation of the PI3K-oxidative
1265 stress axis. *Aging (Albany NY)* **15**, 15196-15212 (2023).
1266 https://doi.org/10.18632/aging.205342

1267 62 Barrett, T. J. Macrophages in Atherosclerosis Regression. *Arterioscler Thromb*
1268 *Vasc Biol* **40**, 20-33 (2020). https://doi.org/10.1161/ATVBAHA.119.312802

1269 63 Scott, T. E. *et al.* IL-4 and IL-13 induce equivalent expression of traditional M2
1270 markers and modulation of reactive oxygen species in human macrophages. *Sci*
1271 *Rep* **13**, 19589 (2023). https://doi.org/10.1038/s41598-023-46237-2

1272 64 Huang, G. *et al.* Potential role of full-length and nonfull-length progranulin in
1273 affecting aortic valve calcification. *J Mol Cell Cardiol* **141**, 93-104 (2020).
1274 https://doi.org/10.1016/j.yjmcc.2020.03.012

1275 65 Saeedi-Boroujeni, A. *et al.* Progranulin (PGRN) as a regulator of inflammation
1276 and a critical factor in the immunopathogenesis of cardiovascular diseases. *J*
1277 *Inflamm (Lond)* **20**, 1 (2023). https://doi.org/10.1186/s12950-023-00327-0

1278 66 Nguyen, A. D. *et al.* Progranulin in the hematopoietic compartment protects
1279 mice from atherosclerosis. *Atherosclerosis* **277**, 145-154 (2018).

1280 https://doi.org/10.1016/j.atherosclerosis.2018.08.042

1281 67 Reifenberg, K. *et al.* Overexpression of TGF-ss1 in macrophages reduces and
1282 stabilizes atherosclerotic plaques in ApoE-deficient mice. *PLoS One* **7**, e40990
1283 (2012). https://doi.org/10.1371/journal.pone.0040990

1284 68 Park, I. *et al.* C-type lectin receptor CLEC4A2 promotes tissue adaptation of
1285 macrophages and protects against atherosclerosis. *Nat Commun* **13**, 215 (2022).
1286 https://doi.org/10.1038/s41467-021-27862-9

1287 69 Chauvin, C. *et al.* Loss of NOD2 in macrophages improves colitis and
1288 tumorigenesis in a lysozyme-dependent manner. *Front Immunol* **14**, 1252979
1289 (2023). https://doi.org/10.3389/fimmu.2023.1252979

1290 70 Alam, M. S. *et al.* Genomic expression analyses reveal lysosomal, innate
1291 immunity proteins, as disease correlates in murine models of a lysosomal
1292 storage disorder. *PLoS One* **7**, e48273 (2012).
1293 https://doi.org/10.1371/journal.pone.0048273

1294 71 Smedbakken, L. M. *et al.* Increased levels of the homeostatic chemokine
1295 CXCL13 in human atherosclerosis - Potential role in plaque stabilization.
1296 *Atherosclerosis* **224**, 266-273 (2012).
1297 https://doi.org/10.1016/j.atherosclerosis.2012.06.071

1298 72 Dangi, A. *et al.* Blocking CCL8-CCR8-Mediated Early Allograft Inflammation
1299 Improves Kidney Transplant Function. *J Am Soc Nephrol* **33**, 1876-1890 (2022).
1300 https://doi.org/10.1681/ASN.2022020139

1301 73 Luo, H., Li, L., Han, S. & Liu, T. The role of monocyte/macrophage chemokines
1302 in pathogenesis of osteoarthritis: A review. *Int J Immunogenet* **51**, 130-142
1303 (2024). https://doi.org/10.1111/iji.12664

1304 74 Ricard, N., Zhang, J., Zhuang, Z. W. & Simons, M. Isoform-Specific Roles of
1305 ERK1 and ERK2 in Arteriogenesis. *Cells* **9** (2019).
1306 https://doi.org/10.3390/cells9010038

1307 75 Al-Ahmadi, W. *et al.* Pro-atherogenic actions of signal transducer and activator
1308 of transcription 1 serine 727 phosphorylation in LDL receptor deficient mice
1309 via modulation of plaque inflammation. *FASEB J* **35**, e21892 (2021).
1310 https://doi.org/10.1096/fj.202100571RR

1311 76 Jin, M. *et al.* Regulation of toll-like receptor (TLR) signaling pathways in
1312 atherosclerosis: from mechanisms to targeted therapeutics. *Acta Pharmacol Sin*
1313 **44**, 2358-2375 (2023). https://doi.org/10.1038/s41401-023-01123-5

1314 77 Frank, J. W., Seo, H., Burghardt, R. C., Bayless, K. J. & Johnson, G. A. ITGAV
1315 (alpha v integrins) bind SPP1 (osteopontin) to support trophoblast cell adhesion.
1316 *Reproduction* **153**, 695-706 (2017). https://doi.org/10.1530/REP-17-0043

1317 78 Erikson, D. W., Burghardt, R. C., Bayless, K. J. & Johnson, G. A. Secreted
1318 phosphoprotein 1 (SPP1, osteopontin) binds to integrin alpha v beta 6 on porcine
1319 trophectoderm cells and integrin alpha v beta 3 on uterine luminal epithelial
1320 cells, and promotes trophectoderm cell adhesion and migration. *Biol Reprod* **81**,
1321 814-825 (2009). https://doi.org/10.1095/biolreprod.109.078600

1322 79 Vallejo, J. *et al.* Activation of immune responses against the basement
1323 membrane component collagen type IV does not affect the development of
1324 atherosclerosis in ApoE-deficient mice. *Sci Rep* **9**, 5964 (2019).
1325 https://doi.org/10.1038/s41598-019-42375-8

1326 80 Li, M. *et al.* Signaling pathways in macrophages: molecular mechanisms and
1327 therapeutic targets. *MedComm (2020)* **4**, e349 (2023).
1328 https://doi.org/10.1002/mco2.349

1329 81 Ruytinx, P., Proost, P., Van Damme, J. & Struyf, S. Chemokine-Induced
1330 Macrophage Polarization in Inflammatory Conditions. *Front Immunol* **9**, 1930
1331 (2018). https://doi.org/10.3389/fimmu.2018.01930

1332 82 Furuhashi, M., Saitoh, S., Shimamoto, K. & Miura, T. Fatty Acid-Binding
1333 Protein 4 (FABP4): Pathophysiological Insights and Potent Clinical Biomarker
1334 of Metabolic and Cardiovascular Diseases. *Clin Med Insights Cardiol* **8**, 23-33
1335 (2014). https://doi.org/10.4137/CMC.S17067

1336 83 Wieczorek, E. *et al.* The Differential Effects of HDL Subpopulations on
1337 Lipoprotein Lipase (LPL)-Mediated VLDL Catabolism. *Biomedicines* **9** (2021).
1338 https://doi.org/10.3390/biomedicines9121839

1339 84 Fang, F. *et al.* Cathepsin K contributed to disturbed flow-induced
1340 atherosclerosis is dependent on integrin-actin cytoskeleton-NF-kappaB pathway.
1341 *Genes Dis* **10**, 583-595 (2023). https://doi.org/10.1016/j.gendis.2022.03.020

1342 85 Zhang, H. *et al.* GPNMB plays an active role in the M1/M2 balance. *Tissue Cell*
1343 **74**, 101683 (2022). https://doi.org/10.1016/j.tice.2021.101683

1344 86 Wang, J. *et al.* Macrophage-derived GPNMB trapped by fibrotic extracellular
1345 matrix promotes pulmonary fibrosis. *Commun Biol* **6**, 136 (2023).
1346 https://doi.org/10.1038/s42003-022-04333-5

1347 87 Nickl, B., Qadri, F. & Bader, M. Role of Gpnmb in atherosclerosis of female

1348 mice. *Biochem Biophys Res Commun* **621**, 20-24 (2022).
1349 https://doi.org/10.1016/j.bbrc.2022.06.082

1350 88 Chen, P. *et al.* Identification and validation of four hub genes involved in the
1351 plaque deterioration of atherosclerosis. *Aging (Albany NY)* **11**, 6469-6489
1352 (2019). https://doi.org/10.18632/aging.102200

1353 89 Huang, K. *et al.* Serum secreted phosphoprotein 1 level is associated with
1354 plaque vulnerability in patients with coronary artery disease. *Front Immunol* **15**,
1355 1285813 (2024). https://doi.org/10.3389/fimmu.2024.1285813

1356 90 Orecchioni, M., Ghosheh, Y., Pramod, A. B. & Ley, K. Macrophage Polarization:
1357 Different Gene Signatures in M1(LPS+) vs. Classically and M2(LPS-) vs.
1358 Alternatively Activated Macrophages. *Front Immunol* **10**, 1084 (2019).
1359 https://doi.org/10.3389/fimmu.2019.01084

1360 91 Collison, J. MMP12 makes the cut. *Nat Rev Rheumatol* **14**, 501 (2018).
1361 https://doi.org/10.1038/s41584-018-0056-y

1362 92 Dean, R. A. *et al.* Macrophage-specific metalloelastase (MMP-12) truncates and
1363 inactivates ELR+ CXC chemokines and generates CCL2, -7, -8, and -13
1364 antagonists: potential role of the macrophage in terminating polymorphonuclear
1365 leukocyte influx. *Blood* **112**, 3455-3464 (2008). https://doi.org/10.1182/blood-
1366 2007-12-129080

1367 93 Willemsen, L. & de Winther, M. P. Macrophage subsets in atherosclerosis as
1368 defined by single-cell technologies. *J Pathol* **250**, 705-714 (2020).
1369 https://doi.org/10.1002/path.5392

1370 94 Chen, Y., Zhang, J., Cui, W. & Silverstein, R. L. CD36, a signaling receptor and
1371 fatty acid transporter that regulates immune cell metabolism and fate. *J Exp Med*
1372 **219** (2022). https://doi.org/10.1084/jem.20211314

1373 95 Herrmann, J., Lerman, L. O., Mukhopadhyay, D., Napoli, C. & Lerman, A.
1374 Angiogenesis in atherogenesis. *Arterioscler Thromb Vasc Biol* **26**, 1948-1957
1375 (2006). https://doi.org/10.1161/01.ATV.0000233387.90257.9b

1376 96 Khurana, R., Simons, M., Martin, J. F. & Zachary, I. C. Role of angiogenesis in
1377 cardiovascular disease: a critical appraisal. *Circulation* **112**, 1813-1824 (2005).
1378 https://doi.org/10.1161/CIRCULATIONAHA.105.535294

1379 97 Asrih, M. *et al.* Overview of growth differentiation factor 15 in metabolic
1380 syndrome. *J Cell Mol Med* **27**, 1157-1167 (2023).
1381 https://doi.org/10.1111/jcmm.17725

1382 98 Adela, R. & Banerjee, S. K. GDF-15 as a Target and Biomarker for Diabetes
1383 and Cardiovascular Diseases: A Translational Prospective. *J Diabetes Res* **2015**,
1384 490842 (2015). https://doi.org/10.1155/2015/490842

1385 99 Kempf, T. *et al.* The transforming growth factor-beta superfamily member
1386 growth-differentiation factor-15 protects the heart from ischemia/reperfusion
1387 injury. *Circ Res* **98**, 351-360 (2006).
1388 https://doi.org/10.1161/01.RES.0000202805.73038.48

1389 100 Preusch, M. R. *et al.* GDF-15 protects from macrophage accumulation in a
1390 mousemodel of advanced atherosclerosis. *Eur J Med Res* **18**, 19 (2013).
1391 https://doi.org/10.1186/2047-783X-18-19

1392 101 Kempf, T. *et al.* GDF-15 is an inhibitor of leukocyte integrin activation required
1393 for survival after myocardial infarction in mice. *Nat Med* **17**, 581-588 (2011).
1394 https://doi.org/10.1038/nm.2354

1395 102 Johnen, H. *et al.* Increased expression of the TGF-b superfamily cytokine MIC-
1396 1/GDF15 protects ApoE(-/-) mice from the development of atherosclerosis.
1397 *Cardiovasc Pathol* **21**, 499-505 (2012).
1398 https://doi.org/10.1016/j.carpath.2012.02.003

1399 103 Chait, A. *et al.* Sexually Dimorphic Relationships Among Saa3 (Serum
1400 Amyloid A3), Inflammation, and Cholesterol Metabolism Modulate
1401 Atherosclerosis in Mice. *Arterioscler Thromb Vasc Biol* **41**, e299-e313 (2021).
1402 https://doi.org/10.1161/ATVBAHA.121.316066

1403 104 den Hartigh, L. J., May, K. S., Zhang, X. S., Chait, A. & Blaser, M. J. Serum
1404 amyloid A and metabolic disease: evidence for a critical role in chronic
1405 inflammatory conditions. *Front Cardiovasc Med* **10**, 1197432 (2023).
1406 https://doi.org/10.3389/fcvm.2023.1197432

1407 105 Reigstad, C. S. & Backhed, F. Microbial regulation of SAA3 expression in
1408 mouse colon and adipose tissue. *Gut Microbes* **1**, 55-57 (2010).
1409 https://doi.org/10.4161/gmic.1.1.10514

1410 106 Jernas, M. *et al.* Separation of human adipocytes by size: hypertrophic fat cells
1411 display distinct gene expression. *FASEB J* **20**, 1540-1542 (2006).
1412 https://doi.org/10.1096/fj.05-5678fje

1413 107 Markle, J. G. *et al.* Sex differences in the gut microbiome drive hormone-
1414 dependent regulation of autoimmunity. *Science* **339**, 1084-1088 (2013).
1415 https://doi.org/10.1126/science.1233521

108 Kaliannan, K. *et al.* Estrogen-mediated gut microbiome alterations influence sexual dimorphism in metabolic syndrome in mice. *Microbiome* **6**, 205 (2018). https://doi.org/10.1186/s40168-018-0587-0

109 Xiao, E. *et al.* Microbiota regulates bone marrow mesenchymal stem cell lineage differentiation and immunomodulation. *Stem Cell Res Ther* **8**, 213 (2017). https://doi.org/10.1186/s13287-017-0670-7

110 Zhang, D. *et al.* The microbiota regulates hematopoietic stem cell fate decisions by controlling iron availability in bone marrow. *Cell Stem Cell* **29**, 232-247 e237 (2022). https://doi.org/10.1016/j.stem.2021.12.009

111 Jylhava, J. *et al.* Serum amyloid A is independently associated with metabolic risk factors but not with early atherosclerosis: the Cardiovascular Risk in Young Finns Study. *J Intern Med* **266**, 286-295 (2009). https://doi.org/10.1111/j.1365-2796.2009.02120.x

112 den Hartigh, L. J. *et al.* Deletion of serum amyloid A3 improves high fat high sucrose diet-induced adipose tissue inflammation and hyperlipidemia in female mice. *PLoS One* **9**, e108564 (2014). https://doi.org/10.1371/journal.pone.0108564

113 Sjoholm, K., Lundgren, M., Olsson, M. & Eriksson, J. W. Association of serum amyloid A levels with adipocyte size and serum levels of adipokines: differences between men and women. *Cytokine* **48**, 260-266 (2009). https://doi.org/10.1016/j.cyto.2009.08.005

114 Cai, X. *et al.* High-Density Lipoprotein (HDL) Inhibits Serum Amyloid A (SAA)-Induced Vascular and Renal Dysfunctions in Apolipoprotein E-Deficient Mice. *Int J Mol Sci* **21** (2020). https://doi.org/10.3390/ijms21041316

Figure 1

a

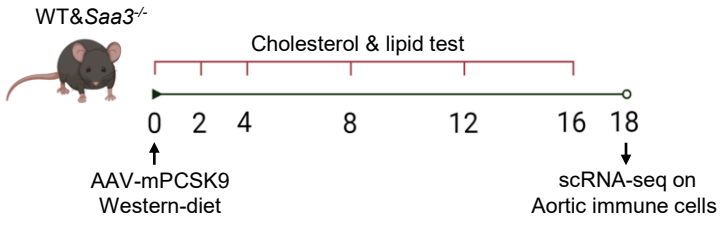

b

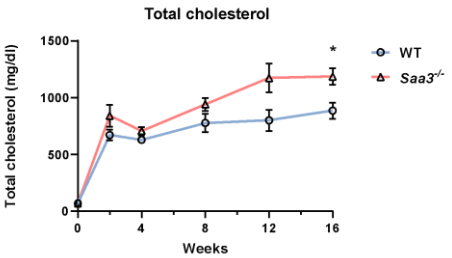

c

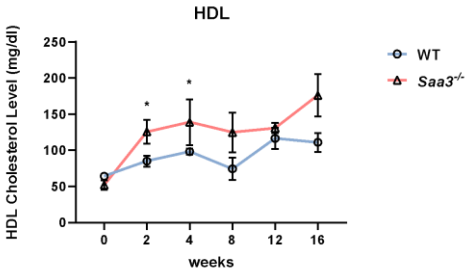

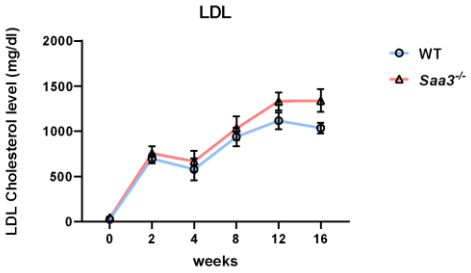

d

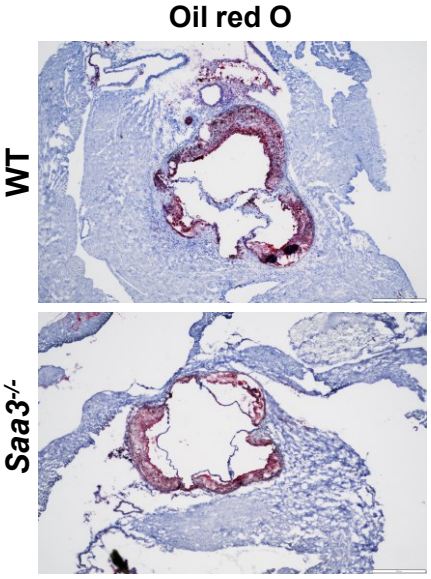

e

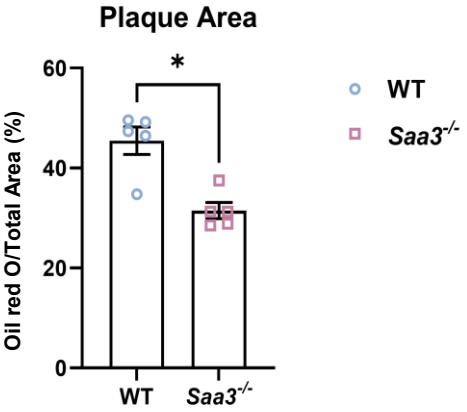

Figure 2

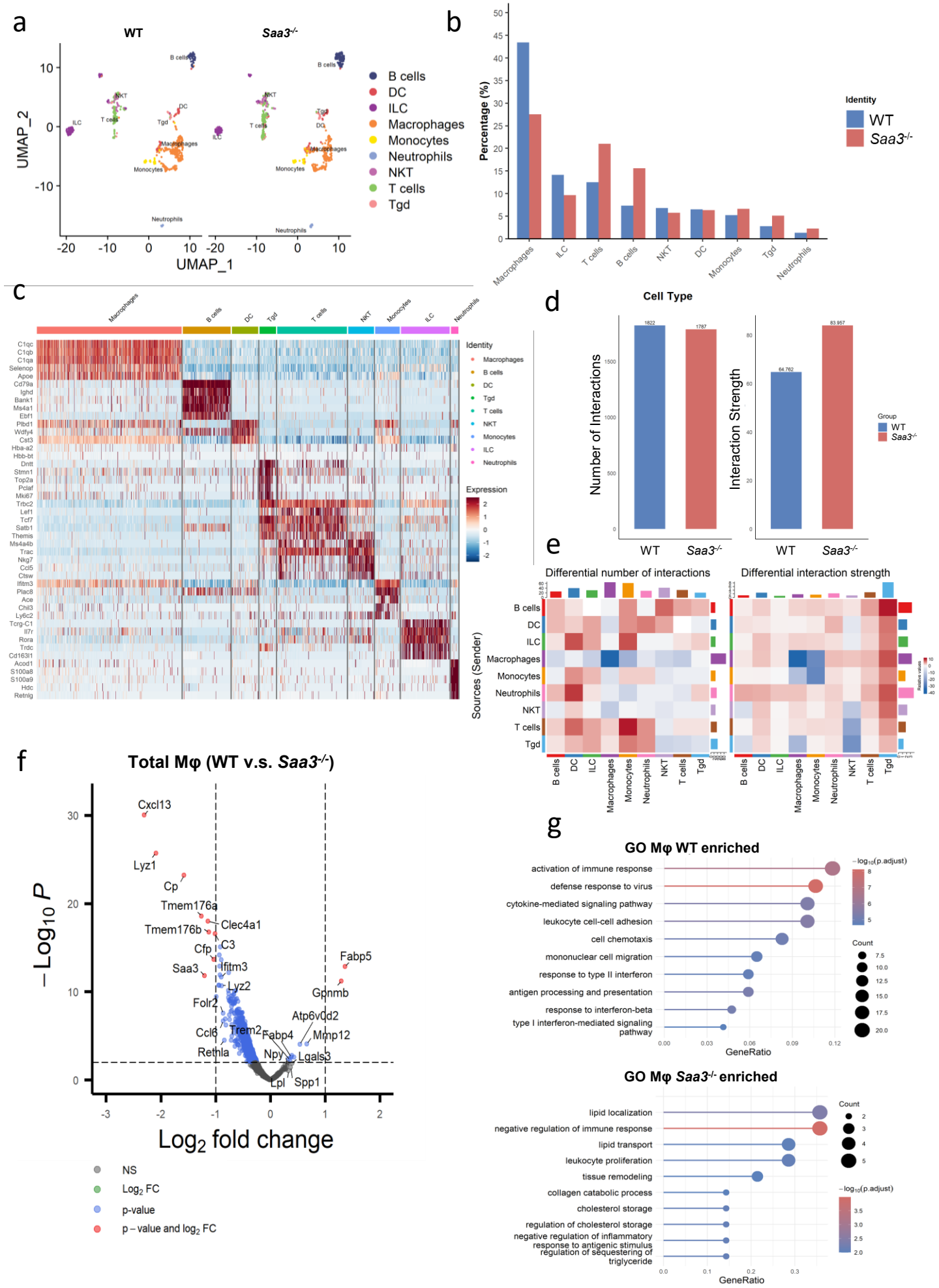
a
WT
Saa3-/-
UMAP_2
UMAP_1
B cells
DC
ILC
Macrophages
Monocytes
Neutrophils
NKT
T cells
Tgd
b
Percentage (%)
Identity
WT
Saa3-/-
c
Identity
Expression
d
Cell Type
Number of Interactions
Interaction Strength
Group
e
Differential number of interactions
Differential interaction strength
Sources (Sender)
f
Total Mφ (WT v.s. Saa3-/-)
−Log10 P
Log2 fold change
Cxcl13
Lyz1
Cp
Tmem176a
Tmem176b
Clec4a1
Cfp
C3
Saa3
Ifitm3
Lyz2
Folr2
Ccl6
Trem2
Fabp4
Rethla
Npy
Lpl
Spp1
Lgals3
Mmp12
Atp6v0d2
Gpnmb
Fabp5
NS
Log2 FC
p-value
p – value and log2 FC
g
GO Mφ WT enriched
activation of immune response
defense response to virus
cytokine-mediated signaling pathway
leukocyte cell-cell adhesion
cell chemotaxis
mononuclear cell migration
response to type II interferon
antigen processing and presentation
response to interferon-beta
type I interferon-mediated signaling pathway
GeneRatio
−log10(p.adjust)
Count
GO Mφ Saa3-/- enriched
lipid localization
negative regulation of immune response
lipid transport
leukocyte proliferation
tissue remodeling
collagen catabolic process
cholesterol storage
regulation of cholesterol storage
negative regulation of inflammatory response to antigenic stimulus
regulation of sequestering of triglyceride

Figure 3

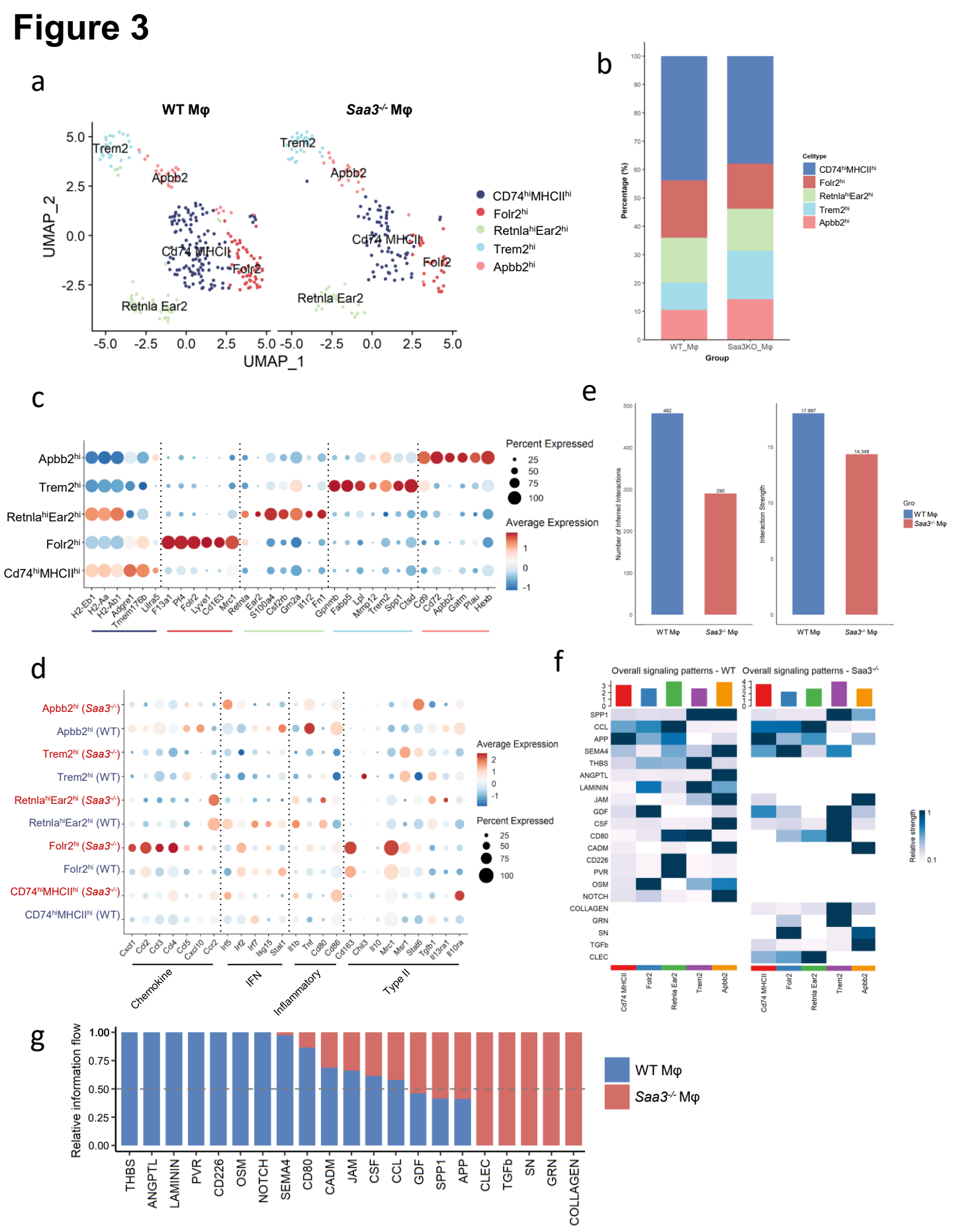
a
WT Mφ
Saa3-/- Mφ
Trem2
Apbb2
Cd74 MHCII
Folr2
Retnla Ear2
UMAP_2
UMAP_1
CD74hiMHCIIhi
Folr2hi
RetnlahiEar2hi
Trem2hi
Apbb2hi
b
Percentage (%)
Group
WT_Mφ
Saa3KO_Mφ
Celltype
c
Percent Expressed
Average Expression
d
Chemokine
IFN
Inflammatory
Type II
e
Number of Inferred Interactions
Interaction Strength
WT Mφ
Saa3-/- Mφ
f
Overall signaling patterns - WT
Overall signaling patterns - Saa3-/-
Relative strength
g
Relative information flow
WT Mφ
Saa3-/- Mφ

Figure 4

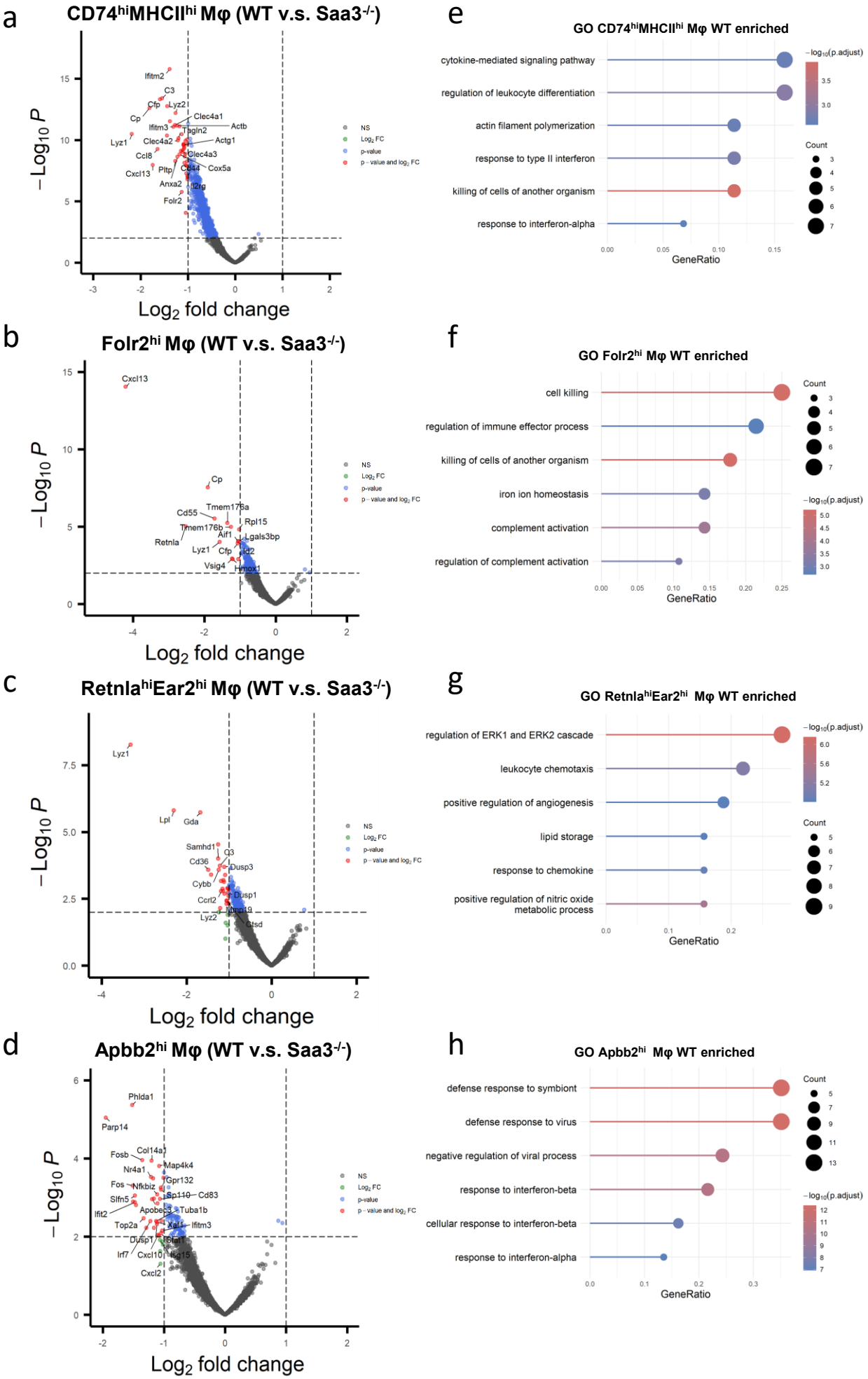
a
CD74hiMHCIIhi Mφ (WT v.s. Saa3-/-)
Ifitm2
C3
Cfp
Lyz2
Cp
Clec4a1
Ifitm3
Actb
Tagln2
Lyz1
Clec4a2
Actg1
Ccl8
Clec4a3
Cxcl13
Pltp
Cd44
Cox5a
Anxa2
Il2rg
Folr2
NS
Log2 FC
p-value
p-value and log2 FC
−Log10 P
Log2 fold change
b
Folr2hi Mφ (WT v.s. Saa3-/-)
Cxcl13
Cp
Tmem176a
Cd55
Rpl15
Tmem176b
Aif1
Lgals3bp
Retnla
Lyz1
Cfp
Id2
Vsig4
Hmox1
c
RetnlahiEar2hi Mφ (WT v.s. Saa3-/-)
Lyz1
Lpl
Gda
Samhd1
C3
Cd36
Dusp3
Cybb
Dusp1
Ccrl2
Dnase1l3
Lyz2
Glsd
d
Apbb2hi Mφ (WT v.s. Saa3-/-)
Phlda1
Parp14
Fosb
Col14a1
Nr4a1
Map4k4
Gpr132
Fos
Nfkbiz
Slfn5
Sp110
Cd83
Ifit2
Apobec3
Tuba1b
Top2a
Xaf1
Ifitm3
Dusp1
Isg15
Irf7
Cxcl10
Cxcl2
e
GO CD74hiMHCIIhi Mφ WT enriched
cytokine-mediated signaling pathway
regulation of leukocyte differentiation
actin filament polymerization
response to type II interferon
killing of cells of another organism
response to interferon-alpha
GeneRatio
−log10(p.adjust)
Count
f
GO Folr2hi Mφ WT enriched
cell killing
regulation of immune effector process
killing of cells of another organism
iron ion homeostasis
complement activation
regulation of complement activation
GeneRatio
Count
−log10(p.adjust)
g
GO RetnlahiEar2hi Mφ WT enriched
regulation of ERK1 and ERK2 cascade
leukocyte chemotaxis
positive regulation of angiogenesis
lipid storage
response to chemokine
positive regulation of nitric oxide metabolic process
GeneRatio
−log10(p.adjust)
Count
h
GO Apbb2hi Mφ WT enriched
defense response to symbiont
defense response to virus
negative regulation of viral process
response to interferon-beta
cellular response to interferon-beta
response to interferon-alpha
GeneRatio
Count
−log10(p.adjust)

Figure 5

a

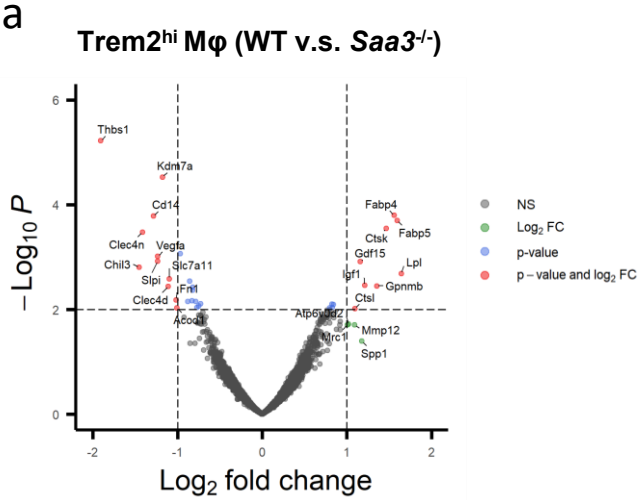

b

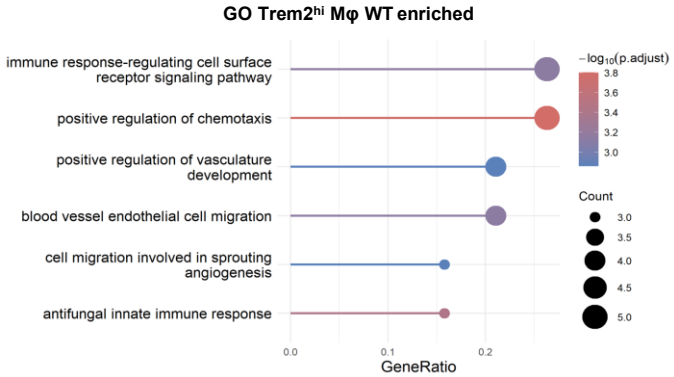

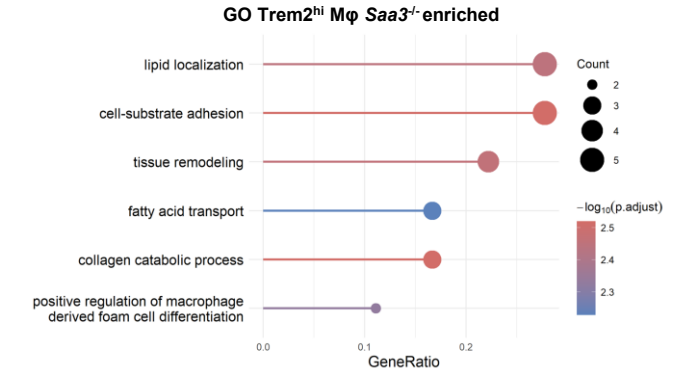

c

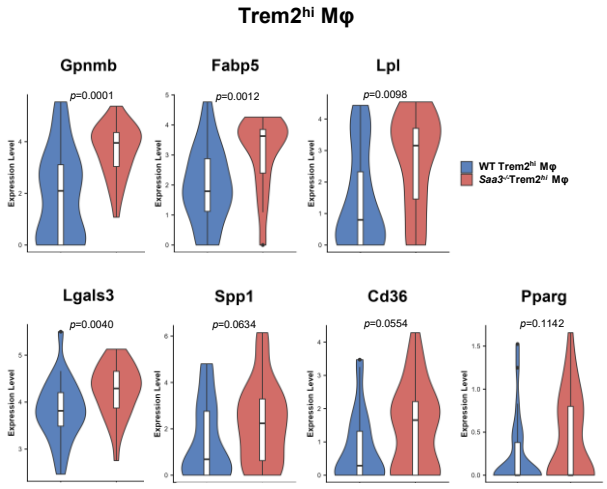

e

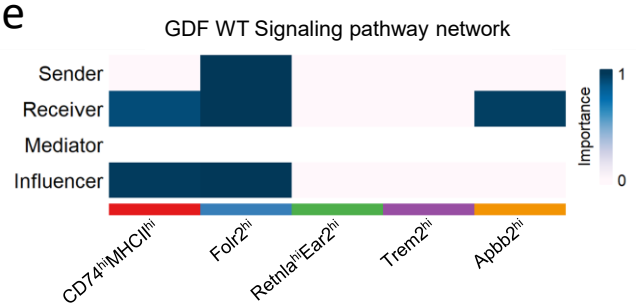

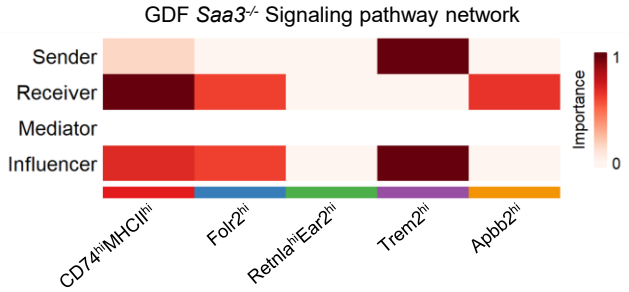

d

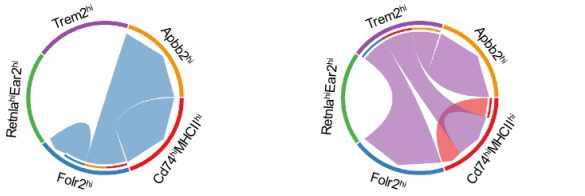

Figure 6

a

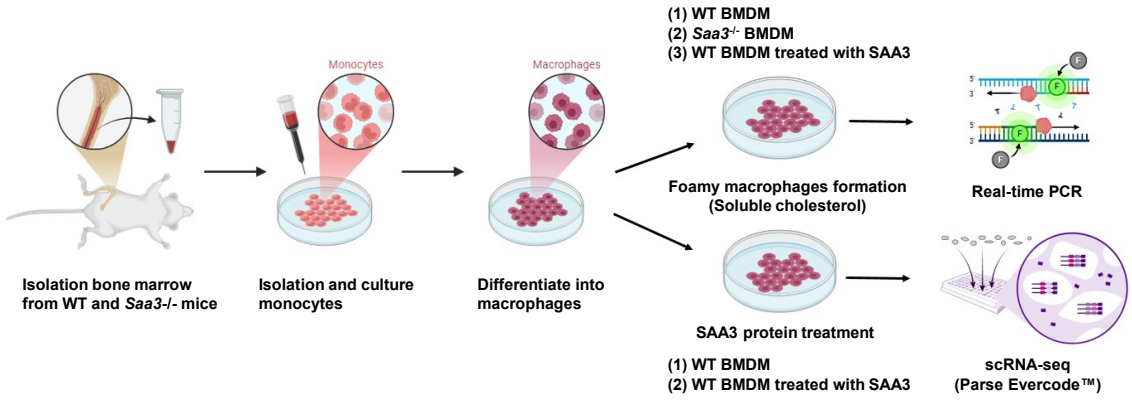

b

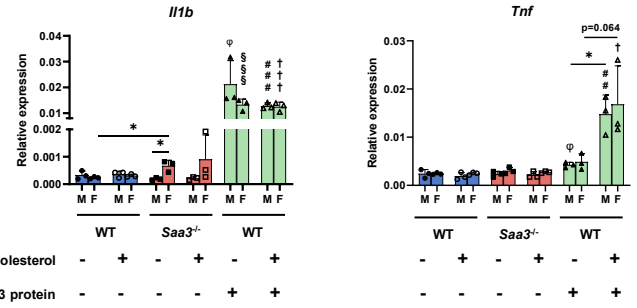

c

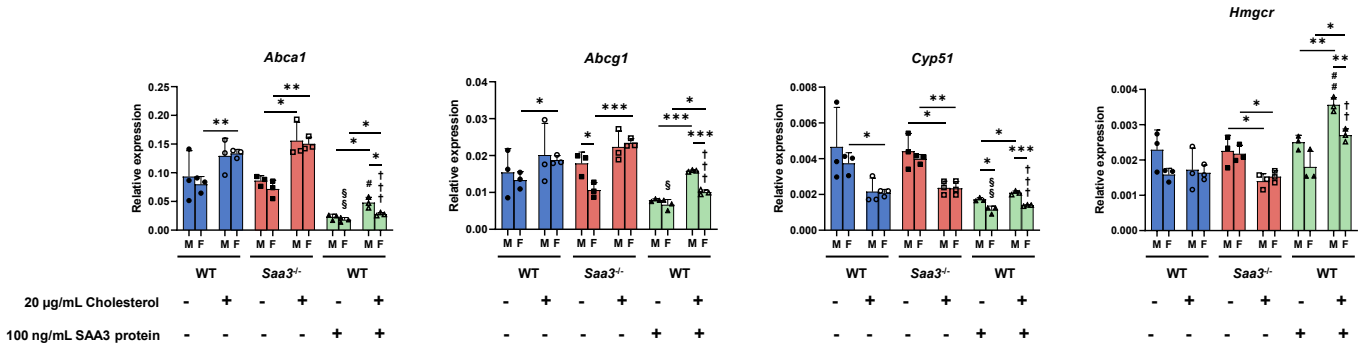

d

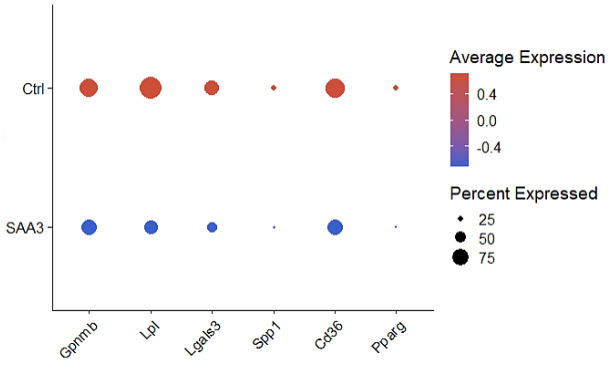

e

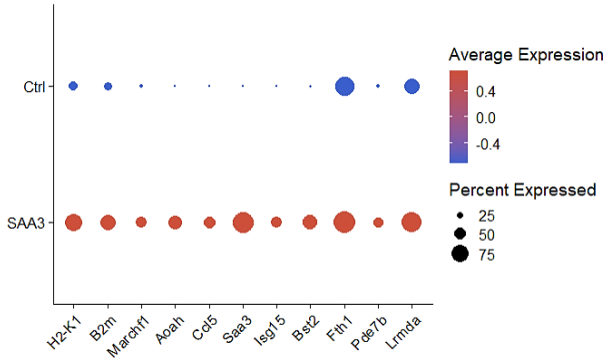

f

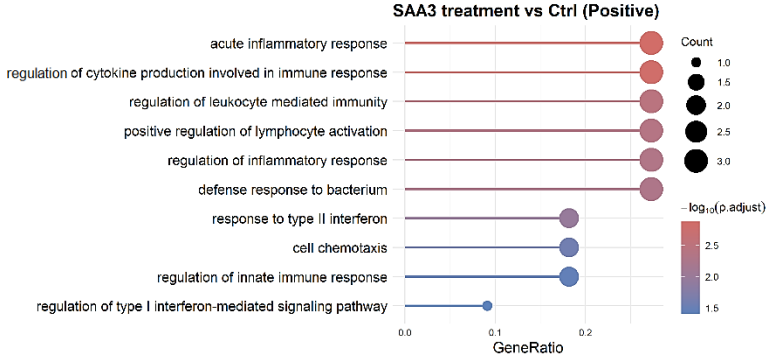

Supplementary Figure 1

a)

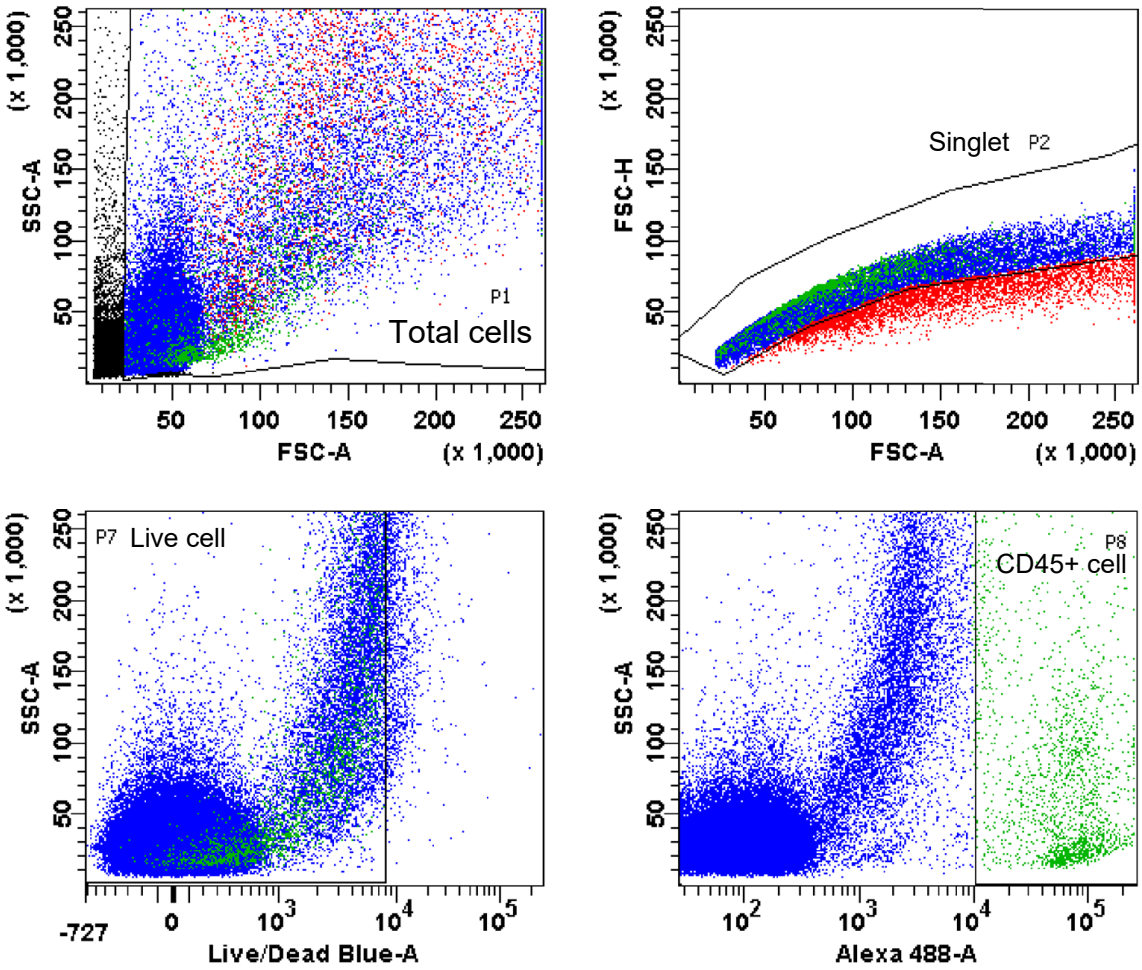

Supplementary Figure 2

a

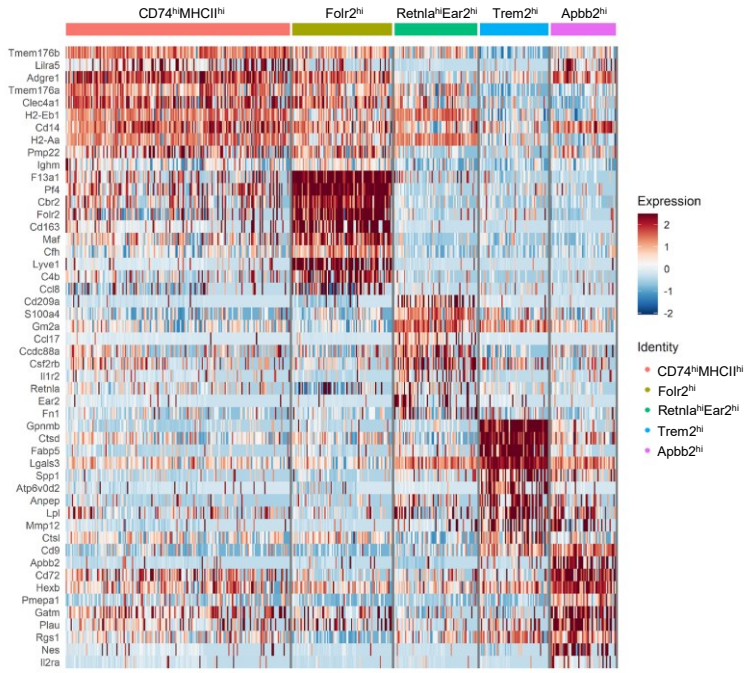

b

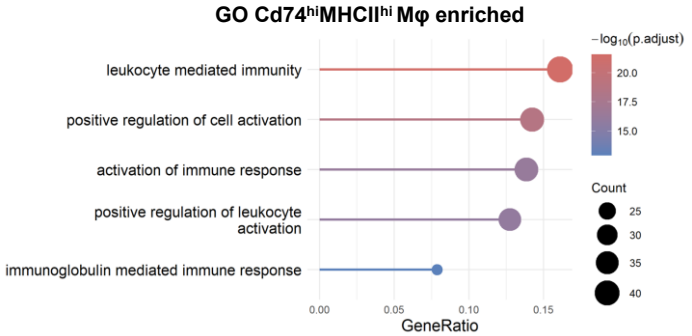

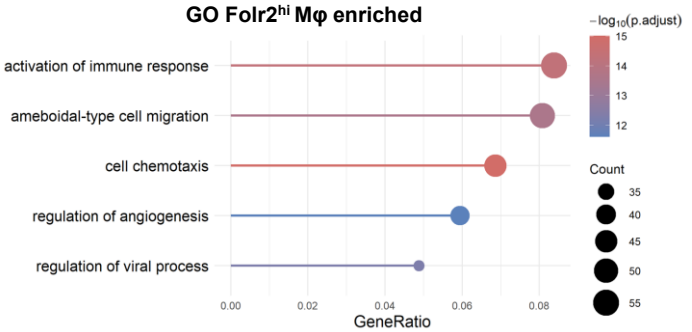

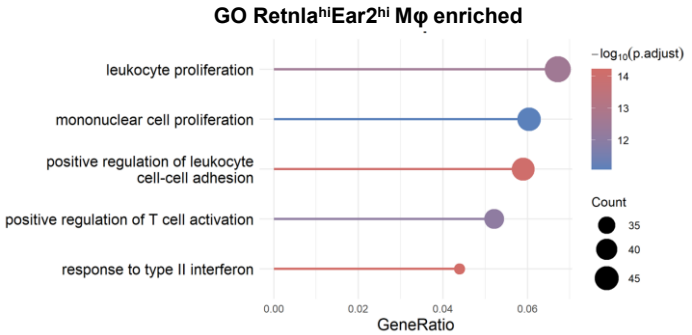

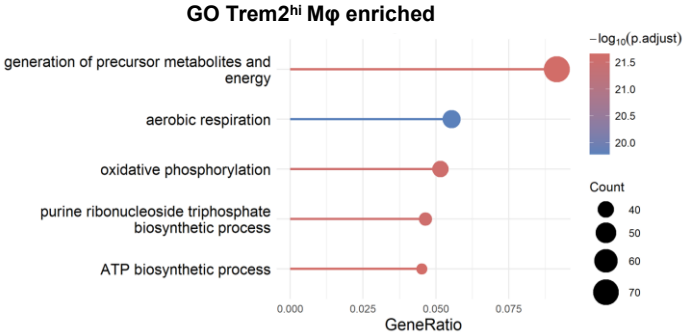

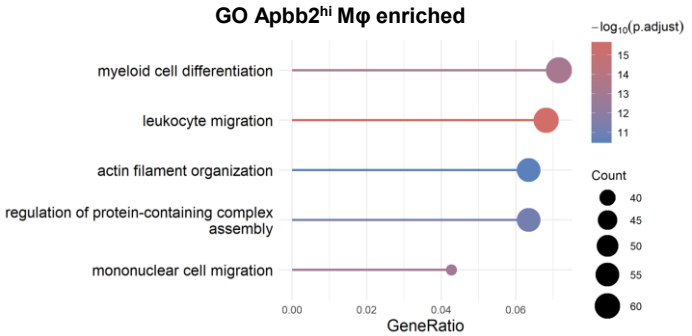

Supplementary Figure 3

a

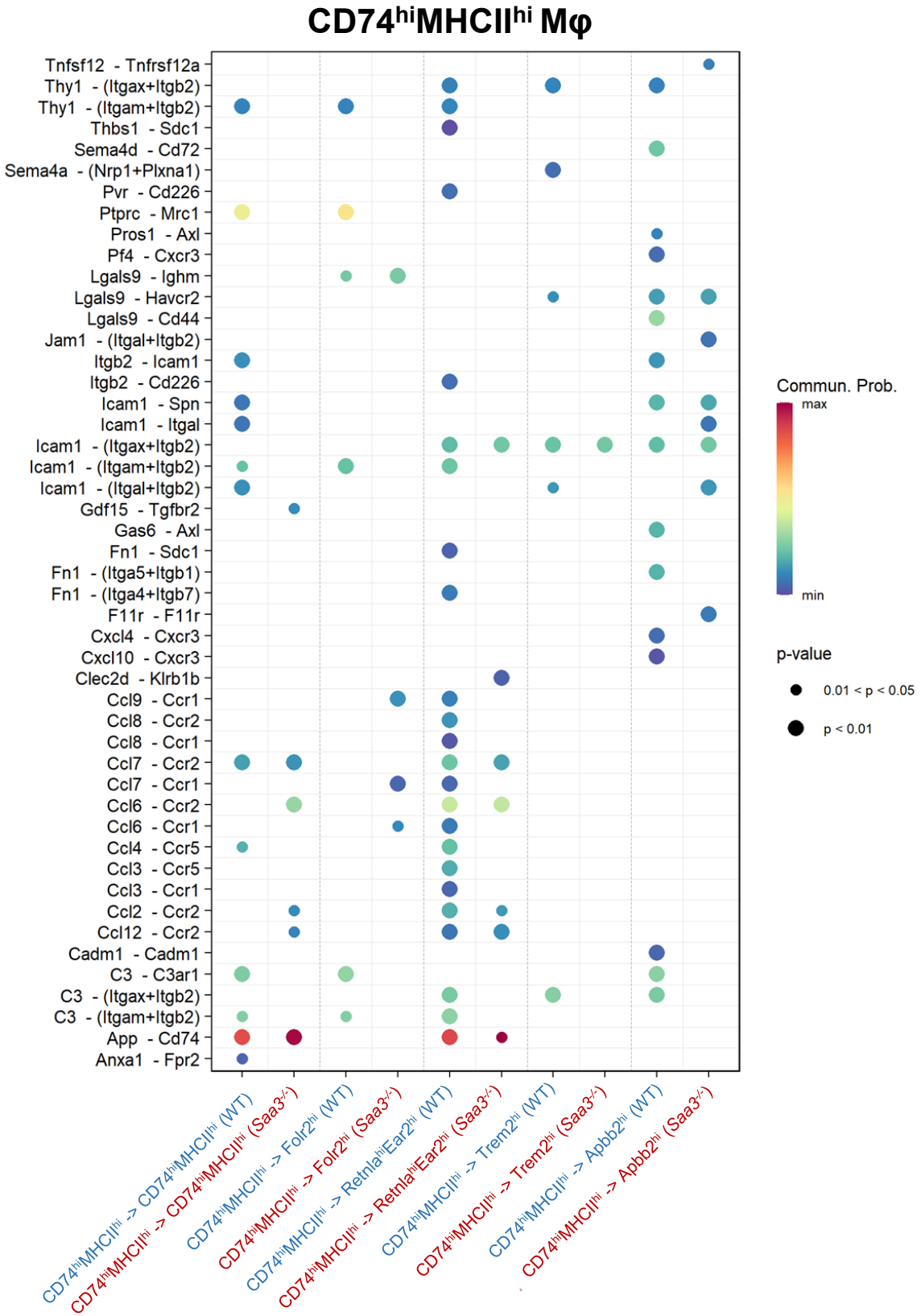

Supplementary Figure 3

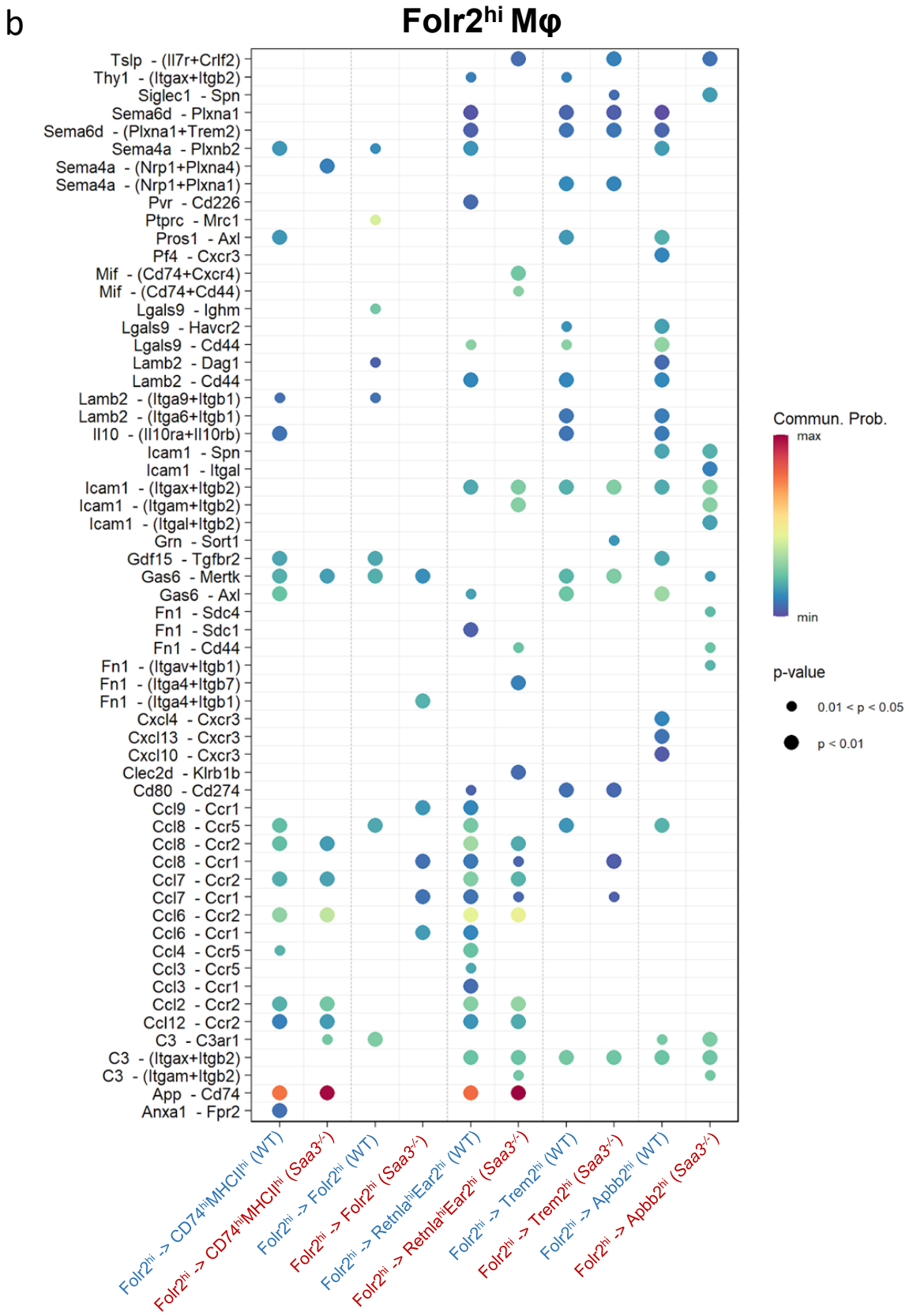

Supplementary Figure 3

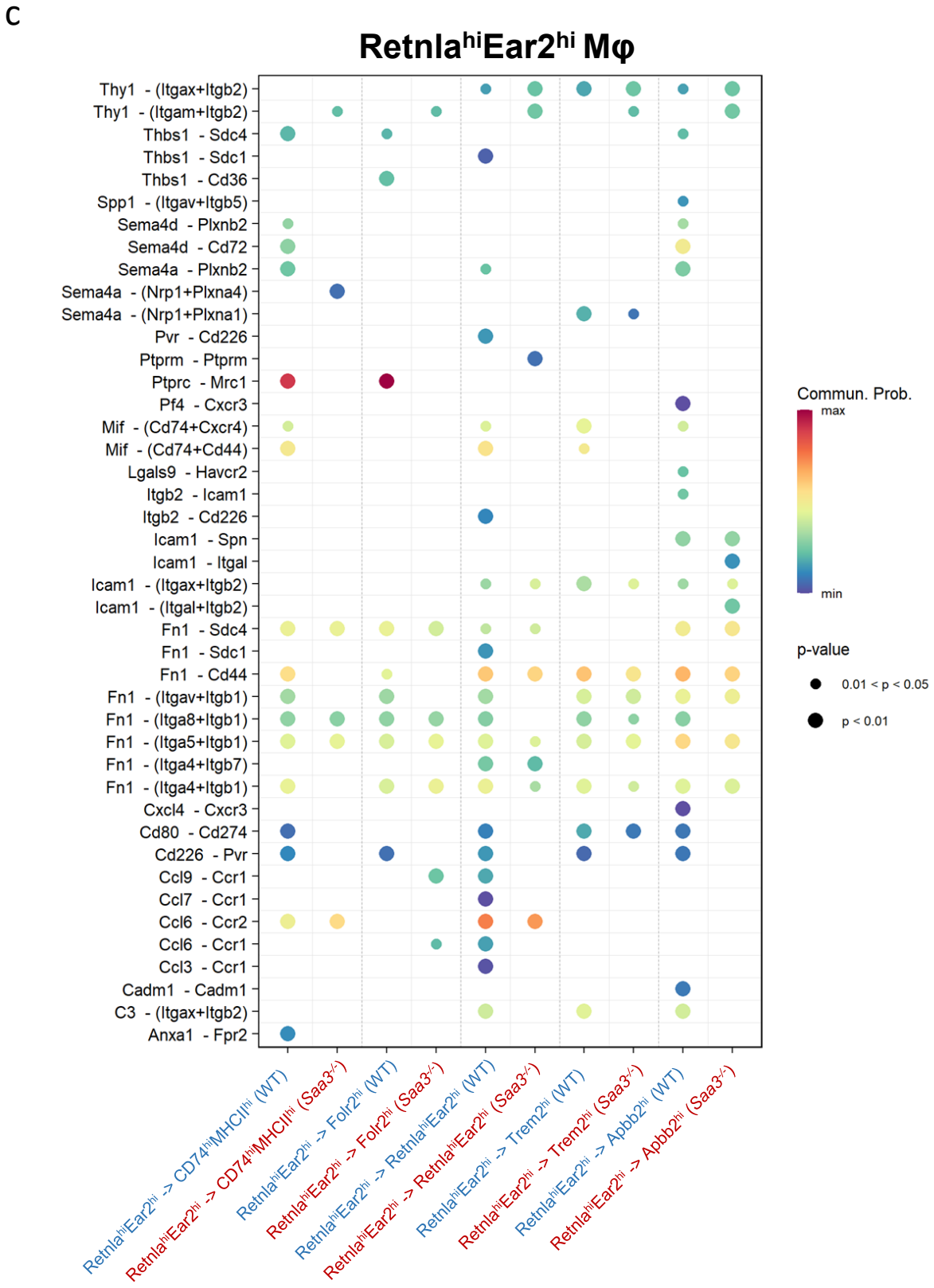

Supplementary Figure 3

d

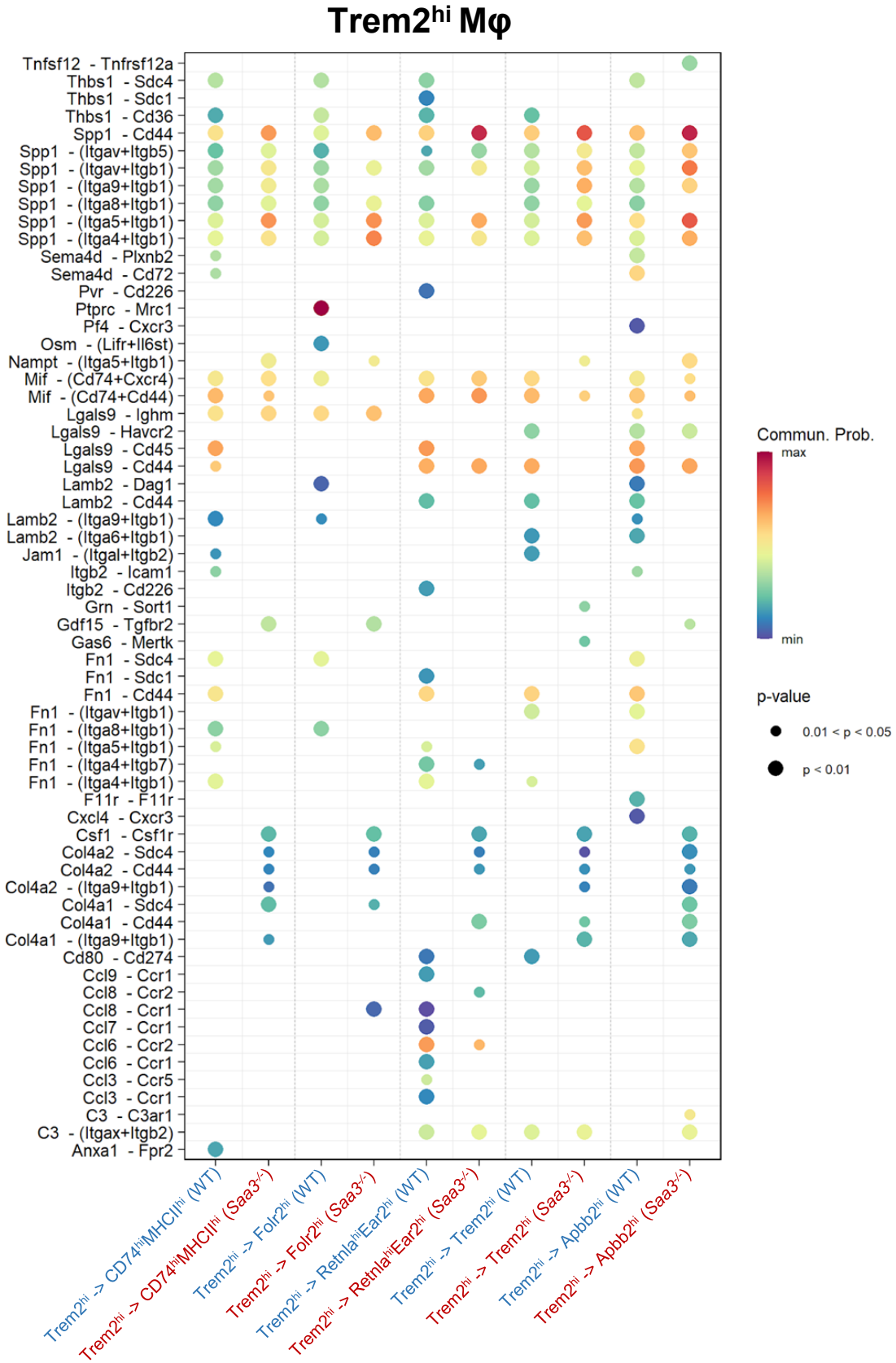

Supplementary Figure 3

e

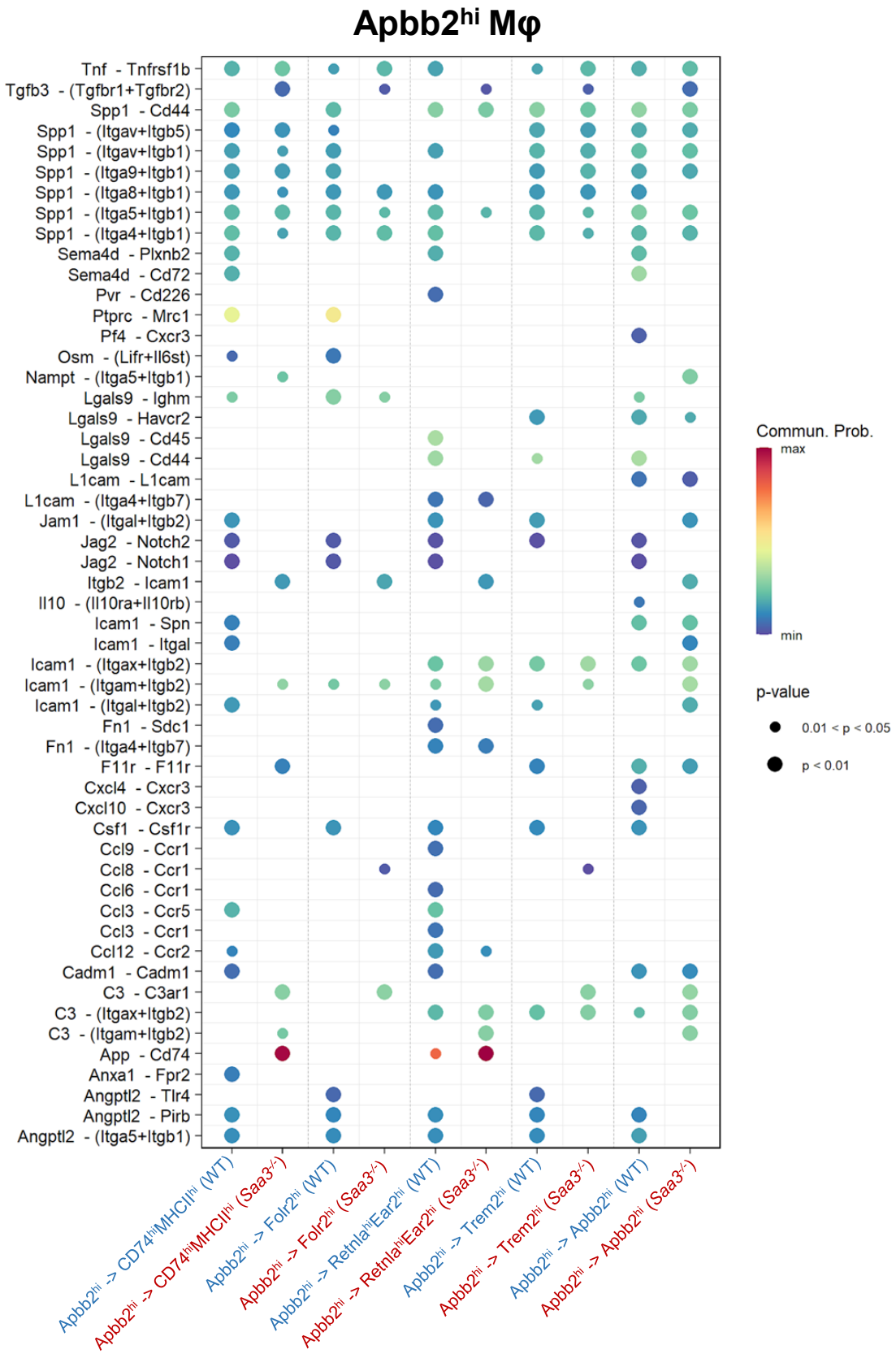
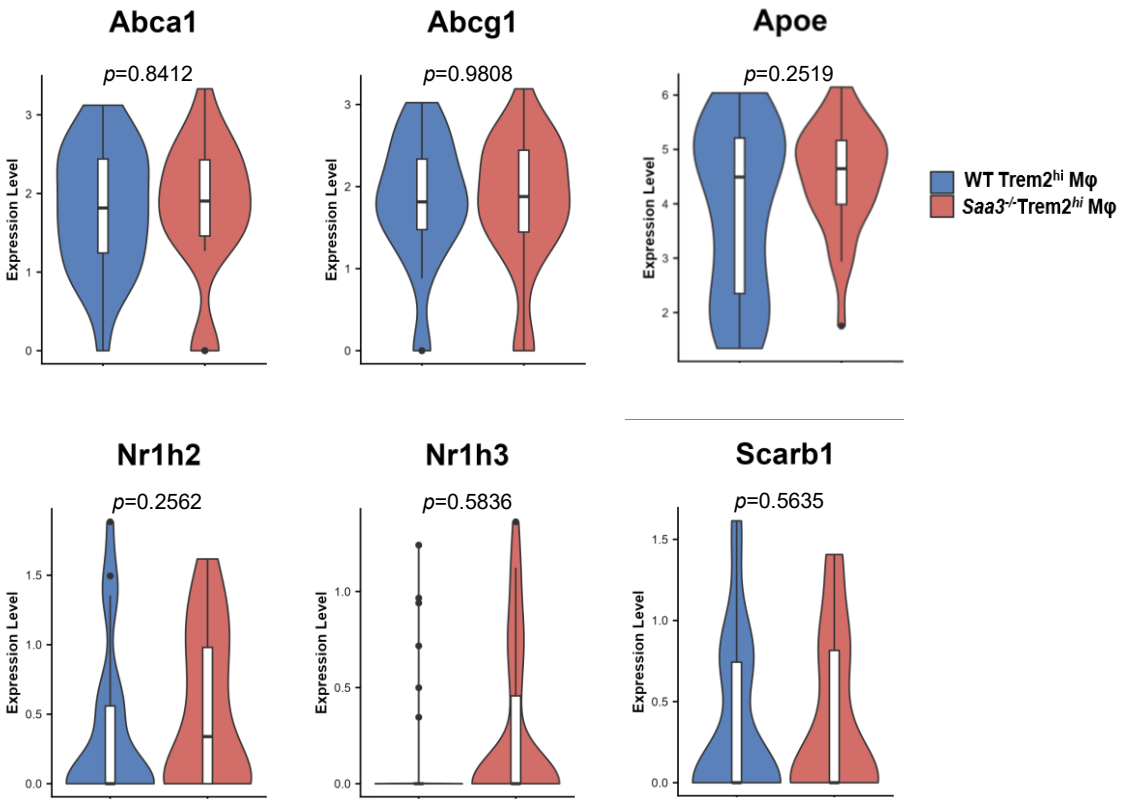
Supplementary Figure 4